ADVANCING EARTH AND SPACE SCIENCE

JGR Atmospheres

RESEARCH ARTICLE
10.1029/2022JD037490

Key Points:

- The regional climate model displays a verifiable intraseasonal variability of precipitation
- The regional climate model simulates the observed unique feature of intraseasonal variations of the monsoon low pressure systems
- The regional climate model shows the observed contrast of convection with warm rain process dominating over ocean compared to that over land

Supporting Information:

Supporting Information may be found in the online version of this article.

Correspondence to:
V. Misra,
vmisra@fsu.edu

Citation:
Misra, V., Jayasankar, C. B., Mishra, A. K., Mitra, A., & Murugavel, P. (2022). Dynamic downscaling the South Asian Summer Monsoon from a global reanalysis using a regional coupled ocean-atmosphere model. *Journal of Geophysical Research: Atmospheres*, *127*, e2022JD037490. https://doi.org/10.1029/2022JD037490

Received 13 JUL 2022
Accepted 28 OCT 2022

Author Contributions:
Conceptualization: Vasubandhu Misra, C. B. Jayasankar, A. K. Mishra
Data curation: Vasubandhu Misra, C. B. Jayasankar
Formal analysis: Vasubandhu Misra
Funding acquisition: Vasubandhu Misra
Methodology: Vasubandhu Misra, C. B. Jayasankar
Project Administration: Vasubandhu Misra
Software: Vasubandhu Misra, C. B. Jayasankar
Validation: Vasubandhu Misra, C. B. Jayasankar
Visualization: Vasubandhu Misra, C. B. Jayasankar, P. Murugavel
Writing – original draft: Vasubandhu Misra, C. B. Jayasankar, A. K. Mishra, P. Murugavel

Dynamic Downscaling the South Asian Summer Monsoon From a Global Reanalysis Using a Regional Coupled Ocean-Atmosphere Model

Vasubandhu Misra[1,2,3], C. B. Jayasankar[2,3], A. K. Mishra[4,5], A. Mitra[5], and P. Murugavel[6,7]

[1]Department of Earth, Ocean and Atmospheric Science, Florida State University, Tallahassee, FL, USA, [2]Center for Ocean-Atmospheric Prediction Studies, Florida State University, Tallahassee, FL, USA, [3]Florida Climate Institute, Florida State University, Tallahassee, FL, USA, [4]Ministry of Earth Sciences, Pune, India, [5]National Center for Medium Range Weather Forecasting, New Delhi, India, [6]Indian Institute of Tropical Meteorology, Pune, India, [7]Savitribai Phule Pune University, Pune, India

Abstract In this study, we present the results of a regional model (regional spectral model-regional ocean model [(RSM-ROMS]) simulation of the South Asian Summer Monsoon (SASM). The RSM-ROMS integration is carried out at 20 km grid spacing over a period of 25 years (1986–2010). The simulation is forced by global atmospheric and oceanic reanalysis. The RSM-ROMS simulation shows a realistic alignment of the simulated rainfall along the orographic features of the domain. Furthermore, the RSM-ROMS simulates the observed feature of convection over continental SASM region being more vigorous with dominance of mixed warm and cold phase hydrometeors in contrast to the dominance of the warm rain process in the neighboring tropical oceans. Similarly, the upper ocean features of contrasting mixed layer and thermocline depths between the northern and equatorial Indian Ocean are also simulated in the RSM-ROMS. Intra-Seasonal Oscillation (ISO) of the SASM at 10–20 and 20–70 days are also simulated in the RSM-ROMS with many of its features verifying with observations. For example, the 20–70 days ISO are of higher amplitude and its meridional propagation is slower in Bay of Bengal compared to that over Arabian Sea. Additionally, RSM-ROMS shows 12.3 Monsoon Low Pressure Systems (LPSs) per season that is comparable to 14.6 per season from observations. Furthermore, the observed intraseasonal contrasts of LPS between the wet and dry spells of ISO is also reproduced in the RSM-ROMS.

Plain Language Summary The South Asian Summer Monsoon (SASM) climate represents a complex mix of variations across many spatio-temporal scales over a region with unique topographic and bathymetric features. As a result, the simulation of the SASM climate offers a stiff challenge to numerical climate models. In this study, we evaluate the added value of a regional coupled ocean-atmosphere model in downscaling the SASM climate from a $2.5° \times 2.5°$ global atmospheric reanalysis and $0.5° \times 0.5°$ global ocean reanalysis to 20 km grid spacing. The regional model demonstrates significant skill in capturing the observed features of the intra-seasonal oscillations of the SASM besides displaying reasonable fidelity of simulating and improving the mean climate of the SASM. Furthermore, at 20 km grid spacing, the regional model simulates the seasonal and intraseasonal activity of the monsoon low pressure systems that is comparable to observations. Therefore, the regional model at 20 km grid spacing of this study clearly demonstrates its added value to its driving global reanalysis in the simulation of the SASM climate, and its intra-seasonal variations. The regional model simulation also demonstrates its fidelity from the verification of the seasonal and intra-seasonal variability of the monsoon low pressure systems of the SASM.

1. Introduction

The South Asian Summer Monsoon (SASM) is one of the most significant sources of terrestrial convection, which exhibits a robust seasonal cycle and is often construed as a significant part of the atmospheric general circulation. The inter-play between the atmosphere and ocean in the evolution of the SASM is complex. It manifests at the interface of ocean-atmosphere and its influence extends well into the free troposphere and much below the ocean surface (Kumar et al., 2005; Loschnigg & Webster, 2000; Misra, 2008; Wang et al., 2003, 2004; Wu & Kirtman, 2005). For example, several studies have suggested that air-sea interaction as displayed by the correlations between atmospheric fluxes and sea surface temperature (SST) is unique to the tropical Indian Ocean

10.1029/2022JD037490

Writing – review & editing: Vasubandhu Misra, C. B. Jayasankar, A. K. Mishra, A. Mitra, P. Murugavel

and plays an important role in the variations of the SASM (Krishnamurti et al., 1988; Sengupta et al., 2001; Wu et al., 2008). Similarly, other studies (e.g., Loschnigg & Webster, 2000; Noska & Misra, 2016) suggest that the interhemispheric transport of heat in the upper ocean (by way of Ekman transport) and in the atmosphere (by way of local Hadley Circulation) nearly balance each other out, regionally over tropical Indian Ocean with the seasonal evolution of SASM.

The sub-seasonal variations of the SASM are significant and is argued to be dominant over other temporal scales of variation (Webster et al., 1998). Webster and Hoyos (2004) suggest that intra-seasonal variations of the SASM precipitation have larger impact on agricultural productivity and water management than interannual variations of the seasonal precipitation anomalies. Although Moron et al. (2012) concluded that SASM precipitation variability is dominated by the interannual timescales with the sub-seasonal variations playing a significant role only during neutral monsoon years. The intra-seasonal variations of the SASM are identified to have two distinct scales of variations with periodicity that is centered around 45 days [often referred as Boreal Summer Intra-Seasonal Oscillation (BSISO)] and 20 days [often referred as quasi-biweekly mode (QBM)] (Krishnamurthy & Shukla, 2007; Krishnamurti & Balme, 1976; Murakami, 1976; Sikka & Gadgil, 1980; Yasunari, 1979, 1980, 1981). A major difference between the BSISO and QBM besides their disparate time scales is in their propagating characteristics. BSISO originates from the equatorial Indian Ocean and propagates northward while the QBM originates from northwest tropical Pacific and propagates northwestward through Bay of Bengal (BoB) to central India. More recently, Karmakar et al. (2021) showed that the genesis of monsoon depressions (MD) is far more prevalent in the active phases of the BSISO than during its inactive spells. Interestingly, it was found that the monsoon lows (ML) were insensitive to the phase of the BSISO.

Despite the familiarity of the SASM phenomenon, the simulation and prediction of the SASM continues to be a challenge. For one, the multi-scale interactions involved in the evolution of the SASM is complex and yet to be fully understood. The role of the local scales of the cumulonimbus clouds to the view of the SASM as a shift of the ITCZ from the equatorial Indian Ocean to the continental region with quasi-divergent planetary circulations make SASM an complex mix of many spatio-temporal scales (Chen et al., 2019, 2021; Goswami, 2005; Meehl, 1987; Webster et al., 1998). Second, the observed anharmonic sub-seasonal variations of the SASM precipitation have been a significant shortcoming feature of many climate models across generations of model development (Ajayamohan et al., 2011; Kang et al., 2002; Konda & Vissa, 2022; Mandke et al., 2020; Rajendran & Kitoh, 2006; Slingo et al., 1996). More recently attempts at simulating the SASM and more importantly its intraseasonal variations at comparatively higher resolutions than global models have been made from regional climate models with limited success (e.g., Bhaskaran et al., 1998; Bhate et al., 2012; Maharana & Dimri, 2016; Samala et al., 2013). It should be noted that most of these regional climate modeling studies of the SASM have been conducted using regional atmospheric models. In some instances where a coupled ocean-atmosphere regional model has been deployed, the lateral boundary conditions to the regional ocean model use climatological monthly mean boundary conditions and/or use some form of flux correction (e.g., Samala et al., 2013; Zou & Zhou, 2016). In contrast, the high-resolution regional climate modeling studies conducted with coupled air-sea interactions of the SASM in Misra et al. (2017) and Misra and Bhardwaj, 2018) in this study use more realistic boundary conditions for the ocean that vary on monthly time scale. These regional climate modeling studies with realistic boundary conditions and coupled air-sea interactions have shown initial promise in simulating the sub-seasonal variations of the SASM. In this study, we are presenting the results of the verification of a 25-year simulation of the SASM conducted with a regional climate model at 20 km grid spacing that includes air-sea coupling. This study is novel in that it is one of the longest integrations conducted at 20 km grid resolution for this region (Figure 1) with a regional coupled air-sea climate model. The resolution and length of the regional climate model integration in this study allows us to also examine the weather extremes of the Monsoon Low Pressure Systems (LPS) and its variations, which was missing from our earlier studies (Misra and Bhardwaj, 2018; Misra et al., 2017).

Verifying the simulation of the downscaling from a global reanalysis is a standard procedure to assess the fidelity of the regional model (Christensen et al., 1997, 2007; Giorgi et al., 2001; Jayasankar et al., 2018; Mearns et al., 2012). This assumes that reanalysis lateral boundary conditions usually have smaller biases than global model simulations, which can otherwise deteriorate the regional model simulation and reflect poorly on the regional model.

Journal of Geophysical Research: Atmospheres 10.1029/2022JD037490

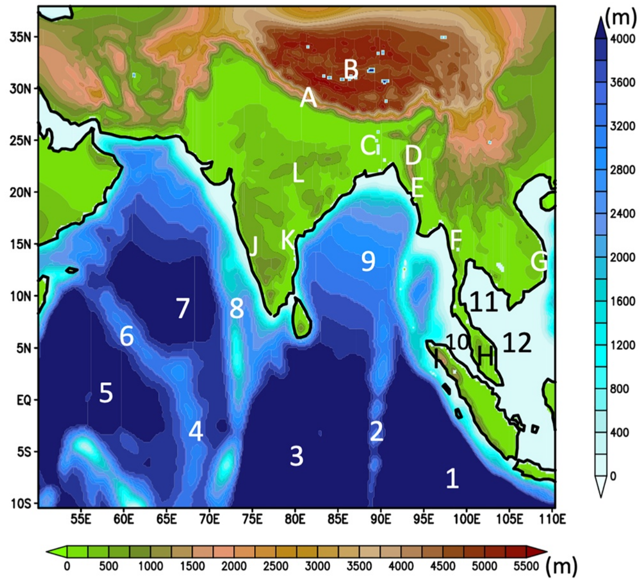

Figure 1. The regional domain of regional spectral model-regional ocean model (RSM-ROMS) with bathymetry and topography (m) shown at 20 km grid spacing with the identification of some of the salient topographic and bathymetric features.

2. Model Description

The model used for this study is the regional spectral model-regional ocean modeling system (RSM-ROMS). RSM-ROMS has been adopted in several climate studies (e.g., Ham et al., 2016; Li et al., 2014a, 2014b; Misra and Bhardwaj, 2018). The RSM is the atmospheric component and ROMS is the oceanic component of the regional coupled ocean-atmosphere modeling system. RSM is based on spectral core using sine and cosine series to solve the primitive equations (Juang & Kanamitsu, 1994). The RSM also uses a spectral damping scheme to reduce climate drift and which also allows for larger than conventional nesting ratios (Kanamaru & Kanamitsu, 2007). In the RSM there are 28 vertical, terrain following $\sigma\left(=\frac{p}{p_s}\right)$ levels reaching up to ~2 hPa. The time step of RSM used in this study is 60 s. A brief outline of the physics adopted in RSM for this study is provided in Table 1.

The choice of the physics package outlined in Table 1 has evolved over time. For example, Misra et al. (2017) experimented with the prognostic cloud scheme. Selman and Misra (2015) tested several cumulus parameterization schemes to arrive at the current choice as indicated in Table 1. The reference data sets, such as the soil type, vegetation type, and vegetation fraction, are interpolated and made consistent with the land ocean mask interpolated to the RSM grid from the Global 30 Arc-Second Elevation (Danielson & Gesch, 2011).

ROMS is a free surface, terrain following primitive equation regional ocean model (Haidvogel et al., 2000; Shchepetkin and McWilliams, 2005). There are 30 vertical stretched terrain (S) levels in ROMS with higher resolution provided in the upper ~500 m of the ocean. The horizontal grid used in ROMS is the staggered Arakawa-C grid. The parameterizations used in ROMS include local closure schemes based on the level 2.5 turbulent kinetic energy equations (Mellor & Yamada, 1982), boundary layer formulation is based on the nonlocal closure scheme (Large et al., Nineteen94), second order biharmonic horizontal diffusion (Ezer et al., 2002), and generic length-scale parameterization (Umlauf & Burchard, 2003). The time step used for ROMS in this study is 300 s.

RSM and ROMS are coupled on identical spatial grids (in cartesian coordinate system) at 20 km grid spacing so that interpolations at their interface and the use of flux coupler is avoided. The size of the domain is 325 grid points in the zonal and 278 grid points in the meridional direction for both RSM

Table 1
Outline of the Physics in Regional Spectral Model (RSM)

Physical parameterization	Reference
Shallow convection	Tiedtke (1983)
Deep convection	Moorthi and Suarez (1992)
Shortwave radiation	Chou and Lee (1996)
Longwave radiation	Chou and Suarez (1994)
Boundary layer	Hong and Pan (1996)
Land surface	Ek et al. (2003)
Gravity wave drag	Alpert et al. (1988)
Clouds (explicit)	Zhao and Carr (1997)

and ROMS. The atmospheric enthalpy, radiation, and momentum fluxes, and SST from the ocean are exchanged between RSM and ROMS at a coupling interval of 1 hr. No flux correction is applied at any point of the integration of RSM-ROMS.

3. Experiment Description and Verification Datasets

A single 25 years integration is conducted with RSM-ROMS over the period of 1986–2010 over the domain indicated in Figure 1. The resolved model topographic and bathymetric features are also shown in Figure 1. The grid spacing at 20 km of RSM-ROMS can resolve many topographical and bathymetric features including the coastal shelf, mesoscale mountain ridges, and valleys. The integration is forced at the lateral boundaries of RSM with NCEP-DOE reanalysis (R2; Kanamitsu et al., 2002) and the lateral boundaries of ROMS is forced with Simple Ocean Data Assimilation v2.2.4 (SODA; Carton & Giese, 2008). It should be noted that this version of SODA reanalysis is available for the 25-year period of 1986–2010, which dictated the period of integration of RSM-ROMS for this study. The newer versions of SODA reanalysis are for more recent but shorter periods. The R2 reanalysis is available at 2.5° grid spacing while SODA is made available at 0.5° grid resolution. The initial conditions of the RSM atmosphere and land surface were obtained from R2 for the corresponding date of the start of the integration. Similarly, the initial conditions for ROMS are obtained from SODA and are not initiated from a state of rest. As a result, the ocean spin-up in RSM-ROMS is not an issue at least for the upper ocean (~300–500 m below the ocean surface). These initial conditions were interpolated to the RSM-ROMS grid at 20 km grid spacing. In this study we verify several variables from RSM-ROMS with many different sources of observation listed in Table S1 in Supporting Information S1 (supplementary material). There are few cases when the validation datasets do not match with the integration period of RSM-ROMS. The seasonal climatology is computed over the months of May–June–July–August–September (MJJAS) season. The extended 5-month season is so chosen to include the earlier onset of the monsoon in South Asia (e.g., Thailand, Cambodia, Myanmar). It may be noted that we linearly interpolate the RSM-ROMS field to the corresponding observed grid whenever differences between them are computed. Otherwise, the fields are plotted on their native grids.

4. Results

4.1. Seasonal Climatology of Upper Air and Surface Meteorological Variables

The observed seasonal climatological rainfall in Figure 2a suggests strong topographic influence. For example, the observed rainfall in Figure 2a shows a maximum along the Western Ghats, in northern BoB, along the northeast Indian Hills, foothills of the Himalayas, the Arakan Yoma and the Bilauktaung Ranges in Myanmar and along the Annamite Range in Laos. There are other moderate, local maxima of rainfall like, over the Vindhya Range in central India and off the Banjaran Titiwangsa Range in Sumatra that clearly mark the influence of the orography on the summer monsoon climatological rainfall (Figure 2a). Similarly, the rain shadow area in southeastern part of India and over Sri Lanka is another manifestation of the orographic influence, which receives less than a tenth of what falls over the Western Ghats or over the Northeast Indian Hills (Figure 2a; Fletcher et al., 2018). These spatial characteristics of the observed MJJAS climatological rainfall are reasonably captured in the RSM-ROMS simulations (Figure 2b), especially in relation to R2 reanalysis (Figure 2c). The pattern correlation coefficient (PCC) of rainfall in RSM-ROMS with respect to IMERG is 0.81 over land and 0.72 over the ocean. The relatively high resolution of the RSM-ROMS simulation at 20 km is certainly helping in focusing the rainfall near orographic features. However, over the Arakan Yoma region, the simulation (Figure 2d) like the R2 reanalysis (Figure 2e) produces a wet bias along coastal Myanmar and a dry bias over the adjacent BoB. But more generally, the rainfall bias over land is reduced in RSM-ROMS compared to R2 reanalysis with the exception over the Himalayas, parts of China, Malay Peninsula and Sumatra. Over the oceans, the dry bias of the RSM-ROMS simulation (Figure 2d) is more extensive (especially over BoB) and the wet bias over southwestern Indian Ocean is more severe than in R2 reanalysis (Figure 2e). However, the rainfall bias in and around Sri Lanka is significantly reduced in RSM-ROMS in relation to R2 reanalysis.

The observed climatology of the MJJAS precipitable water shows a familiar large-scale meridional gradient of decreasing precipitable water from the equatorial Indian Ocean to the Tibetan Plateau and a large-scale positive zonal gradient from the western coast of India across to BoB (Figure 3a). However, this negative meridional gradient of precipitable water is interspersed with a maximum over the northern BoB and the Gangetic-Brahmaputra

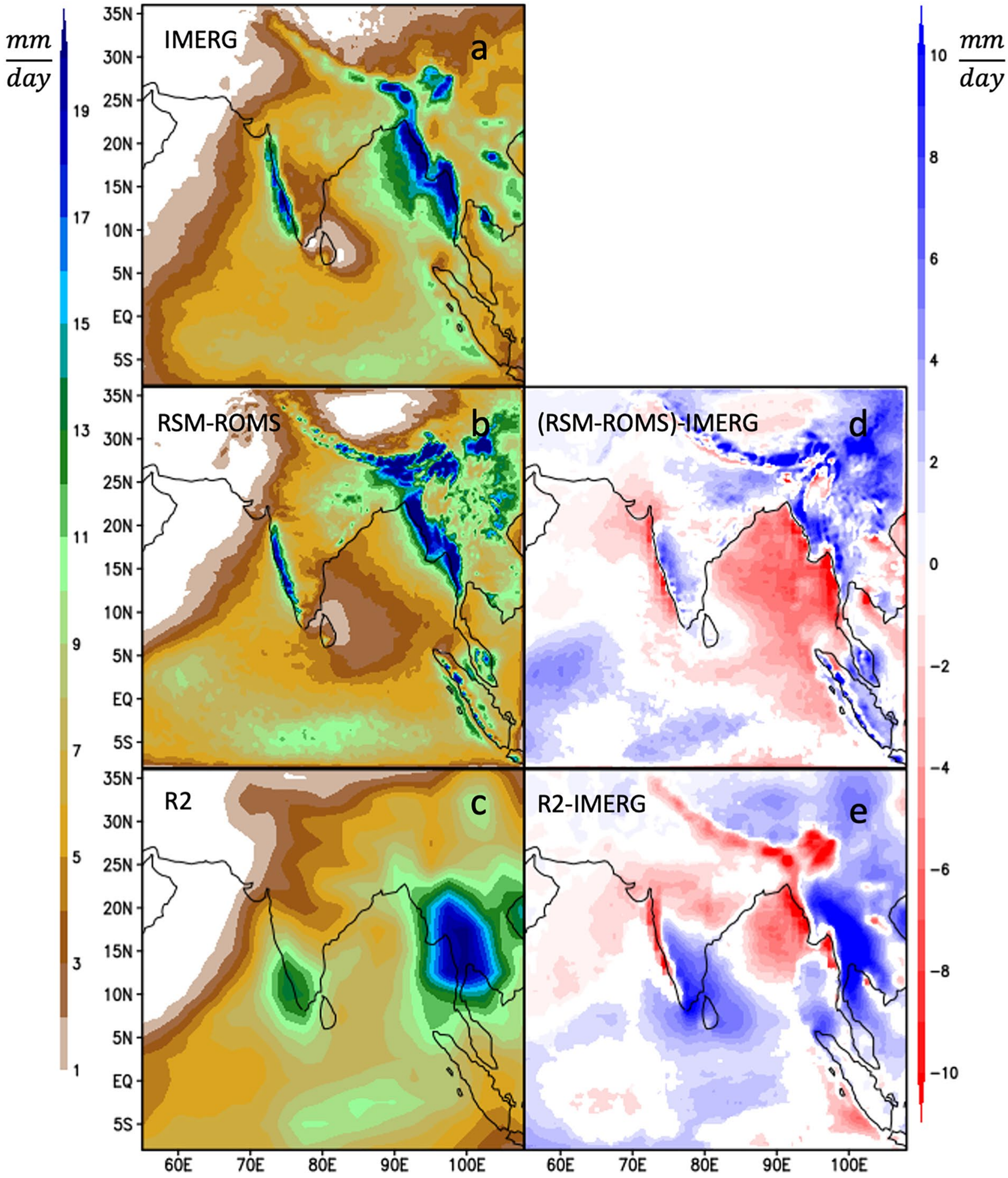

Figure 2. The climatological seasonal (May–June–July–August–September) mean precipitation (mm day^{-1}) from (a) IMERG, (b) regional spectral model-regional ocean model (RSM-ROMS), and (c) R2 reanalysis and the corresponding systematic errors (mm day^{-1}) of (d) RSM-ROMS and (e) R2 reanalysis. Only statistically significant values at 95% confidence interval according to *t*-test is shaded in (d) and (e).

Plain (GBP; Figure 3a). The RSM-ROMS simulation shows these observed gradients although the maxima over the BoB and the GBP is underestimated relative to the ERA5 reanalysis (Figure 3b). This climatological maximum of precipitable water over BoB and GBP and the positive zonal gradient in peninsular India are significantly diminished in the R2 reanalysis (Figure 3c). However, R2 reanalysis preserves the observed broad scale negative meridional gradient of the precipitable water between the equatorial Indian Ocean and the Tibetan Plateau

10.1029/2022JD037490

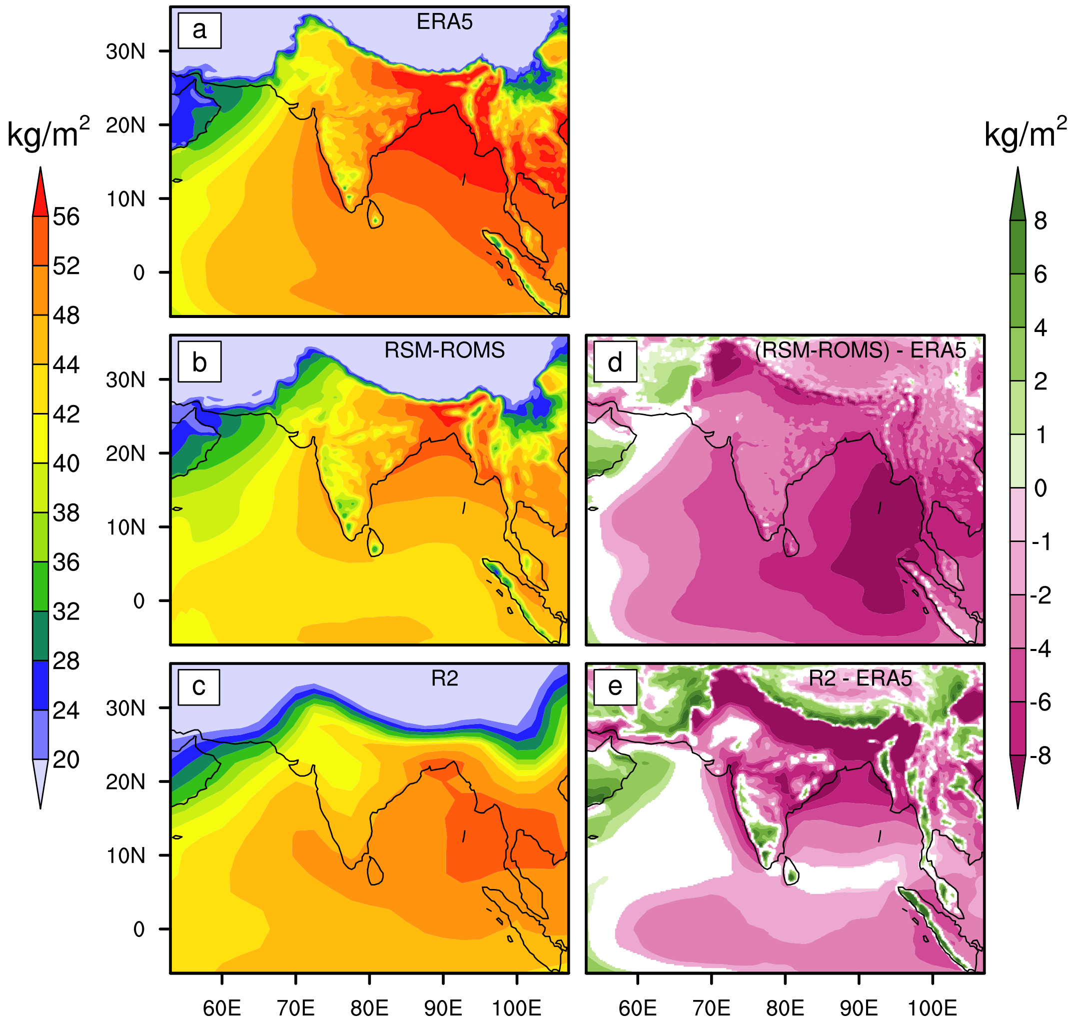

Figure 3. The climatological seasonal (May–June–July–August–September) mean precipitable water (kg m^{-2}) from (a) ERA5, (b) regional spectral model-regional ocean model (RSM-ROMS), and (c) R2 reanalysis and the corresponding systematic errors of (c) RSM-ROMS and (d) R2 reanalysis. Only statistically significant values at 95% confidence interval according to *t*-test is shaded in (d) and (e).

(Figure 3c). The comparison of the systematic errors indicates that the bias of the precipitable water is reduced both over land, especially over the orographic features like the Himalayas and the Vindhya Ranges in central India in RSM-ROMS (Figure 3d) relative to the corresponding moist bias over the Himalayas and dry bias across central India in R2 reanalysis (Figure 3e). The dry bias over the oceans in RSM-ROMS (Figure 3d) is however higher than in R2 reanalysis (Figure 3e). Interestingly, the dry bias in RSM-ROMS is uniform across land and ocean (Figure 3d) unlike in R2 reanalysis (Figure 3e).

The observed characteristics of rainfall of the Indian Summer Monsoon (ISM) reveal that some of the most intense deep convection as witnessed by the frequency of lightning flashes occurs along the Western Ghats, GBP, and the Himalayan Foothills (Murugavel et al., 2021). Furthermore, observations from satellites confirm that thunderstorms in tropical oceans are weaker than those over tropical land surface (Nesbitt et al., 2000; Zipser et al., 2006). Similarly, using passive microwave satellite data, Mohr et al. (1999) showed that ice scattering signatures over land were consistently stronger than over the oceans. It is conjectured that the large difference in the vigor of the convection, between tropical land and ocean could be a result of smaller entrainment rates for land convection (Lucas et al., 1994; Petersen & Rutledge, 1998; Zipser, 2003).

In addition to strong updrafts, lightning activity is engendered by presence of supercooled liquid water and high concentration of frozen hydrometeors (Avila & Caranti, 1994; Williams et al., 2005). Therefore, lightning

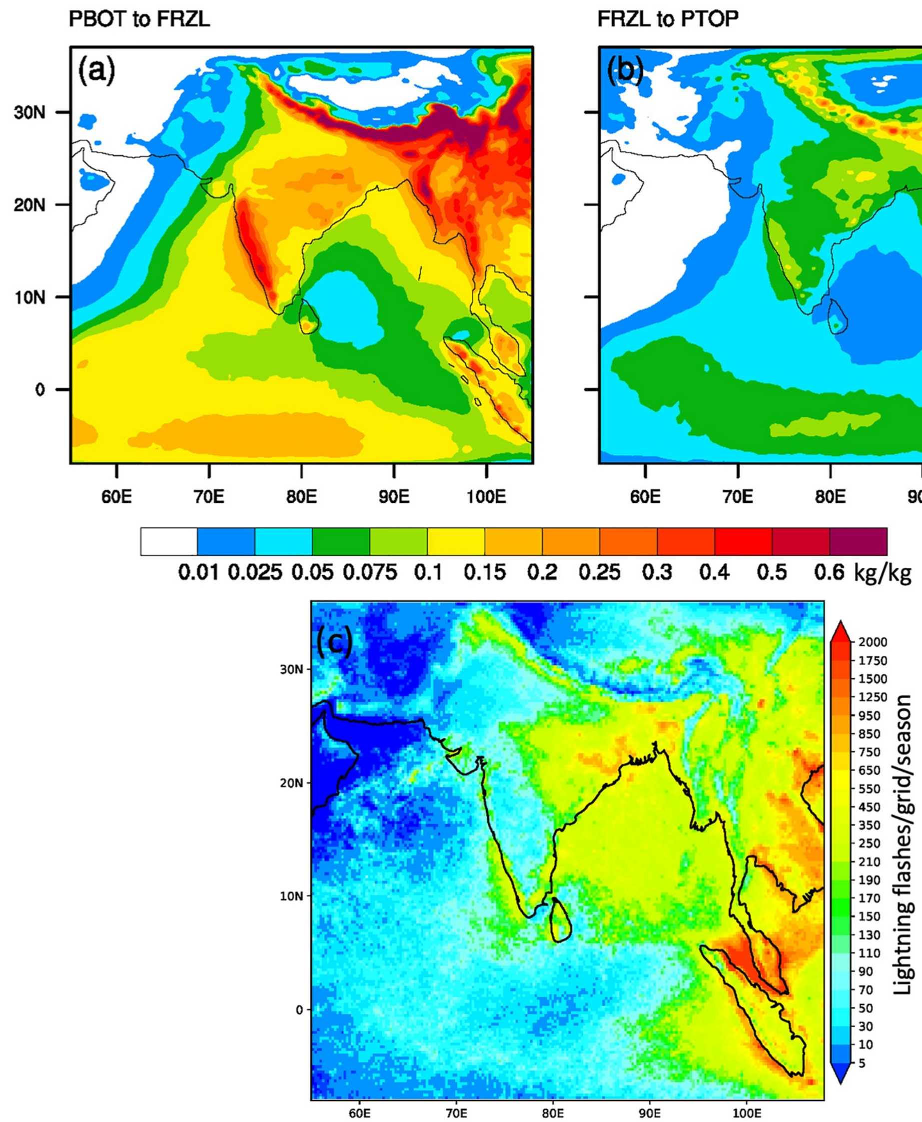

Figure 4. The vertically integrated, seasonal mean (May–June–July–August–September [MJJAS]) climatology of the cloud water content (kg kg^{-1}) between (a) cloud base and freezing level and (b) between freezing level and cloud top from RSM-ROMS. The corresponding MJJAS climatology of lightning flashes from observations are shown in (c).

activity is often used as an indicator of deep convective cells in cloud systems (Carey et al., 2003; Lang & Rutledge, 2002). In Figures 4a and 4b we show the MJJAS climatological mean of the vertically integrated cloud water mixing ratio between surface to freezing level (signifying warm rain process) and from freezing level to top of the atmosphere (signifying cold rain process) in the RSM-ROMS simulation as a proxy to the observed lightning activity (Figure 4c). The cloud water mixing ratio serves as the best proxy from the RSM-ROMS simulation for the presence of hydrometeors above the freezing level since it is the only prognostic water species variable in its cloud microphysics scheme (Zhao & Carr, 1997). Therefore, it is apparent from comparing Figures 4a and 4b and noting the relative abundance of cloud water mixing ratio in RSM-ROMS that deep convection in MJJAS and or lightning activity is more likely over land than in the oceans as the observations would suggest (Figure 4c). Furthermore, by examining the relative abundance of frozen hydrometeors (Figure 4b), the lightning activity in the RSM-ROMS simulation is more likely and frequent in the Western Ghats, Vindhya Range, Northeast Indian Hills, the Himalayan Range, the Arakan Yoma and the Bilauktaung Range in Myanmar and over parts of China than over the rest of the domain as the observations suggest (Figure 4c). The observed lightning strokes in Figure 4c suggests that BoB has far more lightning activity than the rest of the oceans (with the exception over

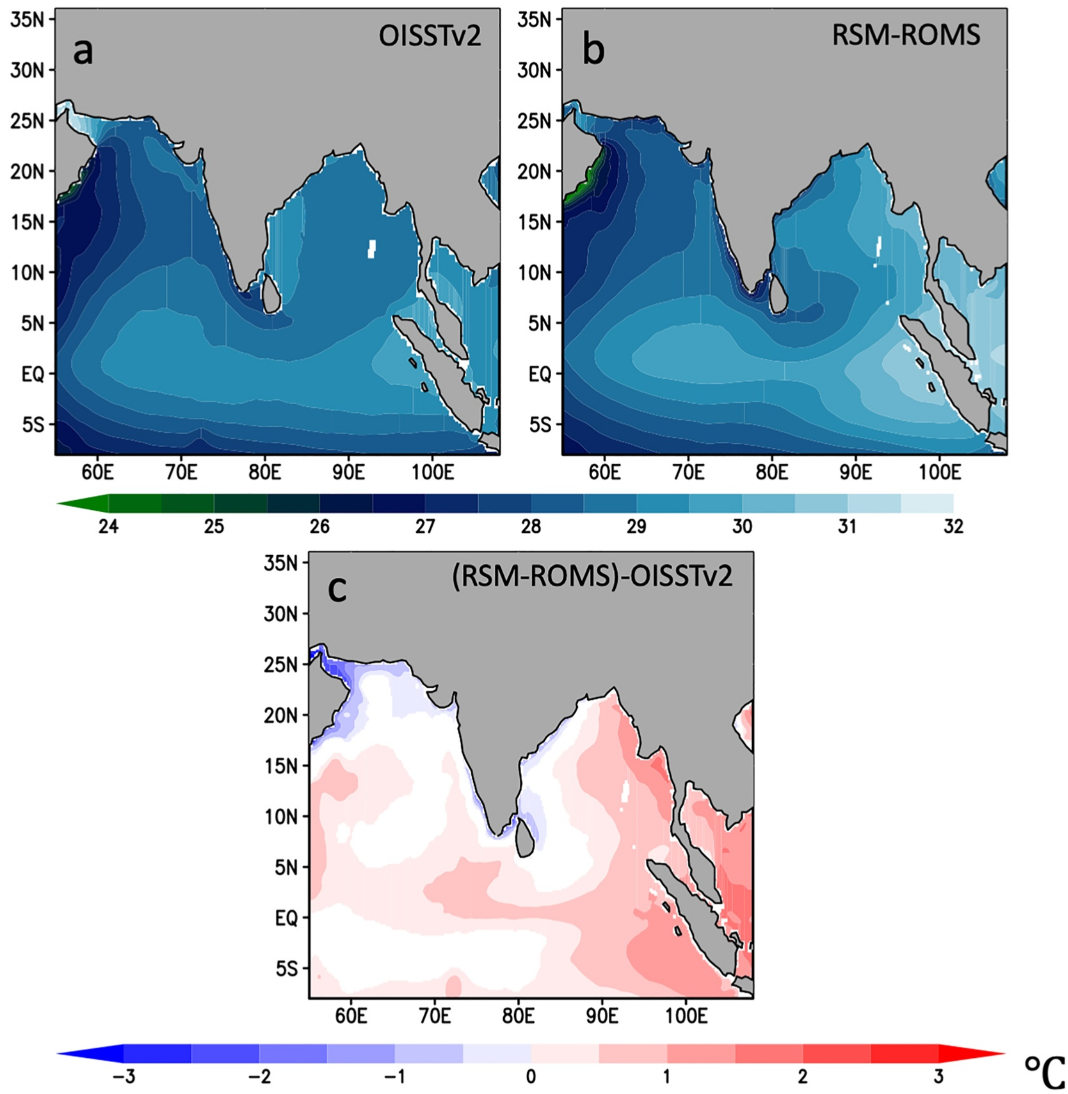

Figure 5. The climatological seasonal (May-June-July-August-September) mean SST (°C) from (a) OISSTv2 and (b) regional spectral model-regional ocean model (RSM-ROMS). (c) The corresponding systematic errors from RSM-ROMS. Only statistically significant values at 95% confidence interval according to *t*-test is shaded in (d) and (e).

Sunda Shelf in Southeast Asia). This distinction of lightning over BoB is not as apparent from the distribution of the frozen hydrometeors in the RSM-ROMS simulation (Figure 4b). The local maximum of lightning in Sunda Shelf is captured in the RSM-ROMS simulation (Figure 4b).

The observed 850 hPa wind climatology of the MJJAS season shows the westerlies over the equatorial Indian Ocean, the strong southwesterlies associated with the Findlater Jet and the monsoon trough residing over the BoB (Figure S1 in Supporting Information S1). The RSM-ROMS reproduces these features (Figure S1b in Supporting Information S1), albeit with a bias of weaker winds of the Findlater Jet and the downstream maximum off the southeastern coast of Sri Lanka. Furthermore, the monsoon trough over the BoB is also weak in the simulation (Figures S1b and S1d in Supporting Information S1). The R2 reanalysis also show similar features with comparable bias as in the RSM-ROMS simulation (Figures S1c and S1e in Supporting Information S1).

4.2. Seasonal Climatology of Upper Ocean Variables

The relatively warm SST across equatorial Indian Ocean and the relatively cold SST along the coastal western Indian Ocean (Figure 5a) is reasonably well replicated in the RSM-ROMS simulation (Figure 5b). These SST

10.1029/2022JD037490

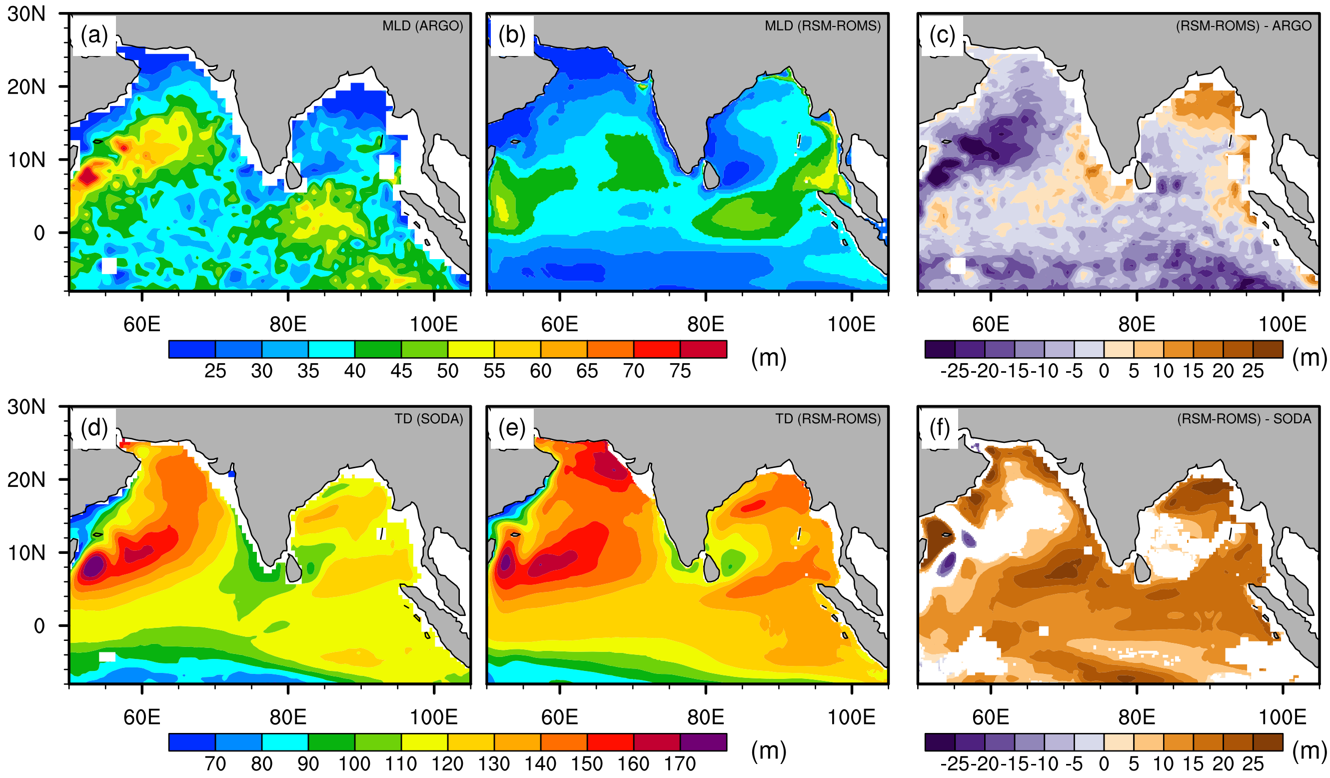

Figure 6. The climatological seasonal (May–June–July–August–September) mean depth (m) of the (a), (b) mixed layer (MLD) (d), (e) 20°C isotherm (20CIso) from (a) Argo, (d) SODA reanalysis, and (b), (e) regional spectral model-regional ocean model (RSM-ROMS). The corresponding systematic errors in the depth of the (c) mixed layer and the (f) 20°C isotherm from the RSM-ROMS simulation. Only statistically significant values at 95% confidence interval according to *t*-test is shaded in (f).

patterns are associated with the weak westerlies along equatorial Indian Ocean and the strong southwesterlies in the western Arabian Sea (AS; Figure S1 in Supporting Information S1). In addition, the wetter and drier conditions that dictate the freshwater influx in equatorial Indian Ocean and western AS, shoal and further deepen the mixed layer depth, respectively. The climatological positive zonal gradient of SST along the equatorial Indian Ocean (Figure 5a) is also simulated in the RSM-ROMS (Figure 5b), albeit, with the gradient being stronger in the latter. The systematic errors of SST in the RSM-ROMS show a warm bias across the eastern Indian Ocean and Gulf of Thailand and along the equatorial Indian Ocean (Figure 5c).

The simulation of the mixed layer depth as diagnosed from the density profile (Monteguet et al., 2004) from RSM-ROMS is compared with corresponding seasonal climatology from Argo in Figures 6a–6c. The Argo observations clearly show the contrasting deeper mixed layer depths over the western AS and the shallower mixed layers depths along the equatorial Indian Ocean and BoB (Figure 6a). The RSM-ROMS simulation in Figure 6b picks this contrast rather weakly. This is largely on account of the underestimation of the mixed layer depth in the western AS (Figure 6c). The depth of the thermocline as diagnosed by the depth of the 20°C isotherm shows that equatorial Indian Ocean has less heat content compared to AS and the BoB (Figure 6d). This feature is replicated in the RSM-ROMS simulation (Figure 6e). Furthermore, the AS displays a higher ocean heat content than the BoB (Figure 6d), which is also demonstrated in the RSM-ROMS simulation (Figure 6e). Although the bias of the excess heat content across the domain in the RSM-ROMS simulation is apparent (Figure 6f).

We also show quantitatively, the fidelity of the SASM climatology in the RSM-ROMS simulation by way of the standardized Taylor diagram in Figure 7. Figure 7 shows that the Pattern Correlation Coefficients (PCCs) of all the variables displayed are around and over 0.69 for both over land and ocean except for the mixed layer depth (0.45), which suggests that RSM-ROMS generally captures the spatial heterogeneity of the variables reasonably well. The upper level winds at 200 hPa followed by precipitable water (Pwat) show comparatively high and comparable PCC between land and ocean relative to other variables (Figure 7). Similarly, the standardized variance is in the vicinity of 1.0 for majority of variables except for SST, precipitation, and zonal wind at 850 hPa,

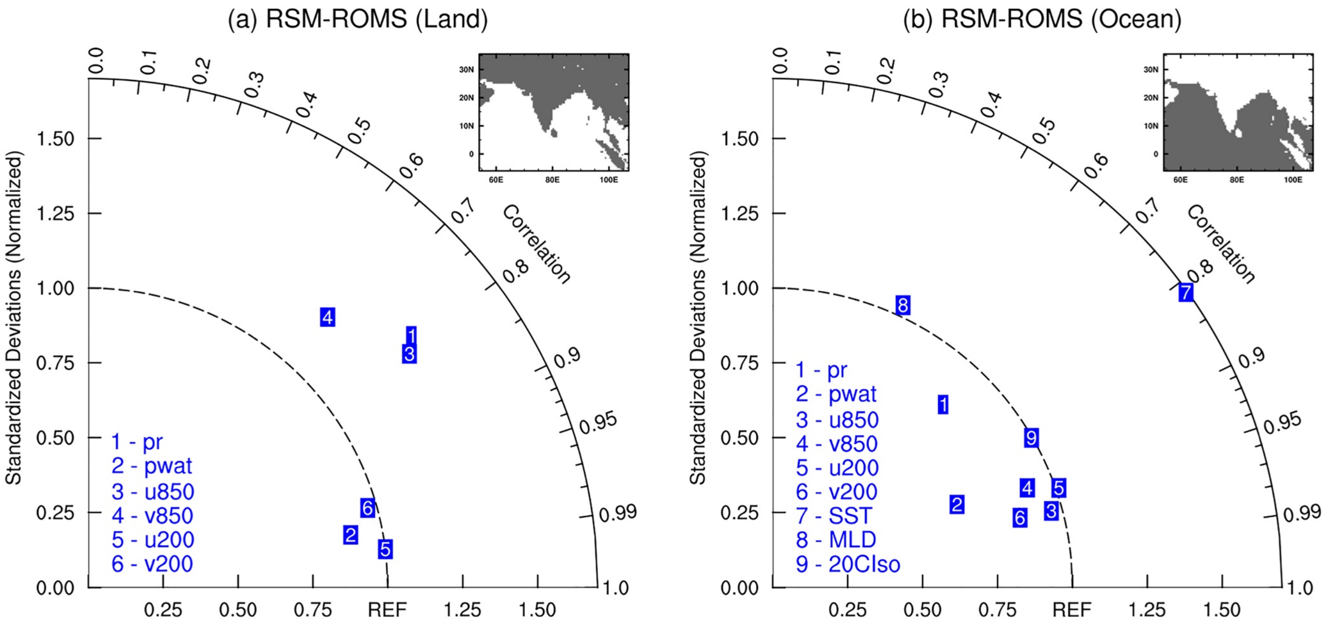

	PCC	Ratio	RMSE
Pr	0.81	1.35	3.66 mm/day
Pwat	0.99	0.91	3.99 kg/m^2
u850	0.83	1.31	2.17 m/s
v850	0.69	1.18	1.88 m/s
u200	0.99	1.00	0.89 m/s
v200	0.98	0.97	0.55 m/s

	PCC	Ratio	RMSE
Pr	0.72	0.81	2.80 mm/day
Pwat	0.93	0.67	5.23 kg/m^2
u850	0.98	0.97	1.00 m/s
v850	0.95	0.92	0.67 m/s
u200	0.96	1.01	1.16 m/s
v200	0.98	0.86	0.67 m/s
SST	0.84	1.68	0.70 C
MLD	0.45	1.00	9.30 m
20CIso	0.89	0.98	14.65 m

Figure 7. Standardized Taylor diagram of the 25-year climatology of May-September mean from regional spectral model-regional ocean model (RSM-ROMS) simulation for precipitation (pr), precipitable water (Pwat), zonal wind at 850 hPa (u850) and at 200 hPa (u200), meridional wind at 850 hPa (v850) and at 200 hPa (v200), for (a) land points of the regional domain and (b) additionally for SST, mixed layer depth (MLD), depth of the 20°C isotherm (20CIso) for ocean points of the regional domain. Here, IMERG, ARGO, and SODA are used as the reference data set for precipitation, MLD, and 20CIso, respectively. ERA5 is used as the reference dataset for the remaining variables. The values of the pattern correlation (PCC), ratio of the standardized variances of model to observations (Ratio), and centered root mean square error (CRMSE) are tabulated.

again suggesting that the spatial variability of the variables is comparable to the corresponding observed values. The centered root mean square error (CRMSE) of the variables in Figure 7 for both over land and ocean is a relatively small fraction of the total field shown earlier in Figures 2–6. Although it may be noted that the CRMSE is averaged across the domain. Even the moisture variables like precipitation and precipitable water that have large spatial and temporal variations appear with reasonably small CRMSE.

4.3. Intraseasonal Variations

The intraseasonal oscillation with its quasi-periodic dry and wet spells is one of the iconic features of the ISM. Using the multi-channel singular spectrum analysis (MSSA; Ghil et al., 2002) we extract the QBM at 10–20 days and BSISO modes at 20–70 day time scales after pre-filtering the daily anomalies of precipitation with a moving five-day mean to remove very high frequency variability (Karmakar & Misra, 2020). Additionally, a bootstrap technique to assess the statistical significance of the isolated intraseasonal oscillations from 1,000 red noise

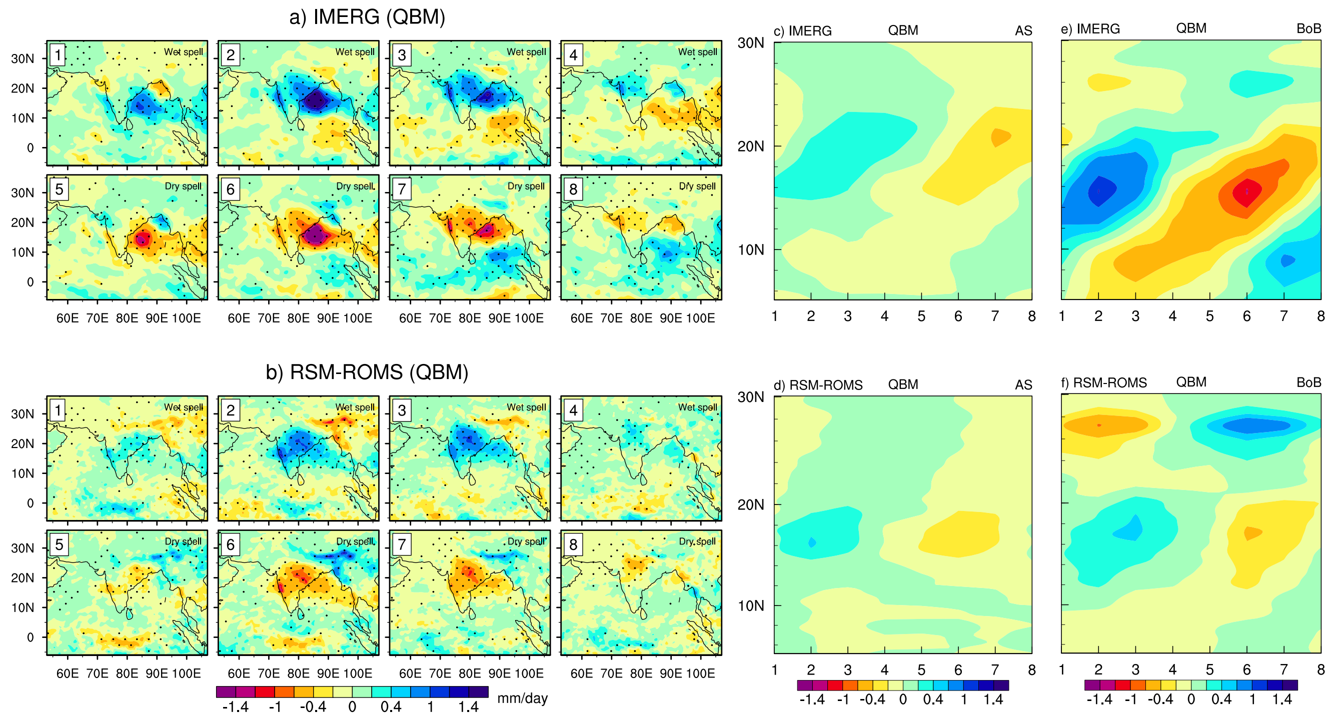

Figure 8. The phase composite diagram of quasi-biweekly mode (QBM) precipitation anomalies (mm day^{-1}) based on April–October period from (a) IMERG and (b) regional spectral model-regional ocean model (RSM-ROMS). Stippled regions indicate anomalies are significant at 5% level using a randomization test following Allen and Robertson (1996). The phase composites are created using area averaged QBM signal over central India (16°N–26°N and 75°E−85°E). The Hovemöller diagram showing the propagation of the precipitation anomalies of the 10–20 days QBM over (c), (d) Arabian Sea (AS; zonally averaged between 65°E and 75°E) and (e), (f) Bay of Bengal filtered (zonally averaged between 85°E and 95°E) from (c), (e) IMERG and (d), (f) RSM-ROMS simulation.

surrogates following Allen and Robertson (1996) is applied to the MSSA. To understand the evolution of the oscillation, a phase composite based on the phase angle of the space time empirical orthogonal functions and principal components from MSSA which lies in the range of 0–2 π is equally divided into eight equal intervals. In the case of QBM and BSISO, each of the phase composites will have a duration between ∼1.25 and 2.5 days and ∼2.5–8.75 days, respectively.

The spatio-temporal evolution of the QBM in precipitation in terms of the phase composites derived from MSSA is shown from observations (Figure 8a) and RSM-ROMS simulation (Figure 8b) using the QBM signal area averaged over central India (16°N–26°N and 75°E−85°E). The first row of four panels (or the first four phase composites of QBM) in Figure 8a indicate wet spell over BoB and central India replaced by a dry spell over the same region in the bottom row of four panels (or the last four phase composites of QBM) in Figure 8a. Similarly, the wet and dry spells of the QBM are indicated in the phase composites of the RSM-ROMS simulation (Figure 8b). The differences in the phase composite of the QBM in RSM-ROMS simulation from observations are apparent in the amplitude and location of the precipitation anomalies. For example, in Figure 8b, the strongest wet and dry spell anomalies of precipitation are located over central India in contrast to the observed anomalies over the open waters of BoB. However, the peak amplitude of the anomalies is observed in Phases 2 and 3 for the wet and Phases 6 and 7 for the dry spell anomalies both in observations (Figure 8a) and model simulation (Figure 8b).

The meridional propagation characteristics of the QBM is highlighted by the Hovemöller (phase-latitude) diagram shown in Figures 8c–8f. Over the AS (zonally averaged between 65°E−75°E), the observations in Figure 8c clearly indicate the northward propagation of QBM by the tilt of precipitation anomalies extending across latitudes. This northward propagation is faster over the AS (Figures 8c and 8d) with the tilt of the anomalies being far more diminished relative to the prominent tilt signifying slower northward propagation over the BoB longitudes (zonally averaged between 85°E and 95°E; Figures 8e and 8f). However, unlike the observations, the meridional propagation of the QBM over the AS is over a shorter latitude span in RSM-ROMS (Figure 8d)

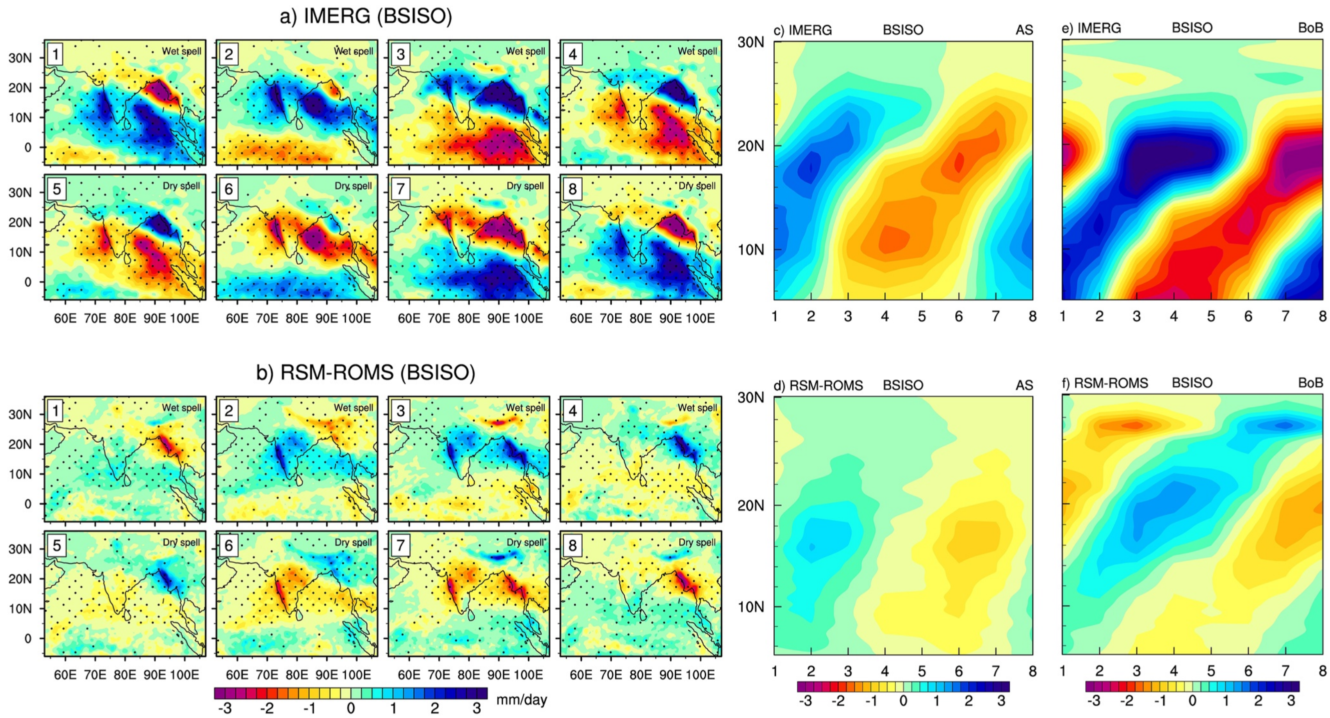

Figure 9. The phase composite diagram of BSISO precipitation anomalies (mm day^{-1}) based on April–October period from (a) IMERG and (b) regional spectral model-regional ocean model (RSM-ROMS). Stippled regions indicate anomalies are significant at 5% level using a randomization test following Allen and Robertson (1996). The Hovemöller diagram showing the propagation of the precipitation anomalies of the BSISO over (c), (d) Arabian Sea (AS; zonally averaged between 65°E−75°E) and (e), (f) Bay of Bengal filtered (zonally averaged between 85°E−95°E) from (c), (e) IMERG and (d), (f) RSM-ROMS simulation.

compared to observations (Figure 8c). Additionally, the QBM anomalies south of 12°N in BoB are much weaker in RSM-ROMS (Figure 8f) compared to observations (Figure 8e).

The phase composites of BSISO are shown in Figures 9a and 9b, which are significantly stronger than the QBM composite anomalies (Figures 8a and 8b). Once again, the phase composites in Figures 9a and 9b are based on the BSISO signal, area averaged over central India (16°N–26°N and 75°E−85°E). The propagation of the BSISO in the observations is apparent in Figure 9a with Phases 1, 2, 3, and 4 marking the northward progression of the wet spell across the latitudes of the Indian subcontinent and southeast Asia while simultaneously marking the northward progression of the dry spell over the Indian Ocean from south of the equator across to ∼8°N. In Phases 5, 6, 7, and 8 the precipitation anomalies change sign with wet spell south of 8°N and dry spell north of this latitude (Figure 9a). The RSM-ROMS simulation produces these observed features of the BSISO in Figure 9b with the amplitude of the anomalies slightly weaker than observations. The RSM-ROMS simulation also correctly shows the amplitude of the BSISO anomalies to be stronger than those of the QBM anomalies. An important feature of the BSISO is the northwest-southeast tilt, which is a result of the faster propagation of the convection anomalies in the AS relative to BoB (Karmakar & Misra, 2020). This tilt in the BSISO anomalies is apparent both in the observations and in the RSM-ROMS simulation (Figures 9a and 9b). The meridional phase propagation characteristics of the BSISO indeed indicate that the northward propagation over the AS longitudes (Figures 9c and 9d) is faster than in the BoB (Figures 9e and 9f). These propagation characteristics of the BSISO have been the "Achilles heel" for most climate models including the latest round of CMIP6 models (Konda & Vissa, 2022). However, the simulation tends to significantly diminish the BSISO anomalies north of 20°N over the AS while extending robustly further north over BoB in comparison to observations.

4.4. Monsoon Low Pressure Systems

LPS is a major component of the SASM, contributing nearly half of the total seasonal rainfall in large parts of South Asia (Hunt & Fletcher, 2019; Yoon & Chen, 2005). In South Asia, weaker LPS are typically called Monsoon Lows (ML; wind speeds about 8.5 m/s with one closed isobar of mean sea level pressure [MSLP]) and stronger ones are called Monsoon Depressions (MD; wind speeds are in the range 8.5–13.4 m/s with two or three closed isobars of MSLP at 2 hPa interval). Typically, we observe about 14 LPS over the ISM of which, about 10 are ML, 2.5 are MD, and 1.5 are deep depressions (>13.4 m/s with two or three closed isobars of MSLP at 2 hPa interval; Sikka, 2006). Hurley and Boos (2015) further revised these figures using ERA-Interim analysis (Dee et al., 2011) to suggest that on average during the ISM there are about 16 LPS with ∼4 MD, and fewer than 1 deep depression. More recently, Vishnu et al. (2020) compared five other global reanalyses including ERA5. They noted some diversity in the LPS counts across reanalysis. But ERA5 was found to have closest match to the analysis of LPS following Sikka (2006). Furthermore, Vishnu et al. (2020) notes an improvement in the seasonal cycle of the LPS in ERA5 relative to other reanalysis when verified with the seasonal cycle of LPS in Sikka (2006).

The TempestExtremes algorithm of Ullrich and Zarzycki (2016) is used to track the LPS from the ERA5 reanalysis and RSM-ROMS during June to September over the 25 year period from 1986 to 2010 (Figure 10). We used data at 6-hourly interval for estimating the LPS track information. The LPS are detected based on the 850 hPa geopotential criteria as mentioned in Vishnu et al. (2020), in which they consider the ML/MD as a disturbance to have 850 hPa geopotential that increases by 125 m^2s^{-2} from the center minimum within a radius of 10° (Figures 10a and 10b). Additionally, the tracks are considered only if it achieves an 850 hPa relative humidity of at least 85% for at least 1 day (average of the four-time steps of 6-hourly interval of data) and a surface geopotential of less than 8,000 m^2s^{-2}. ML in Figures 10d and 10e are categorized by further considering the 10-m wind speeds, which are less than or up to 8.5 ms^{-1} with one closed isobar of MSLP. MD in Figures 10g and 10h are further based on 10-m wind speeds greater than 8.5 ms^{-1} and with greater than two closed isobars of MSLP at 2 hPa interval.

Over the 25 year period from 1986 to 2010, 366 and 307 LPS were detected with an average of 14.6 per season and 12.3 per season in ERA5 (Figure 11a) and in the RSM-ROMS simulation (Figure 10b), respectively. The track densities of the LPS in RSM-ROMS (Figure 10b) shows the familiar northwest-southeast orientation extending from the head of BoB to northern India (Figure 10a). However, RSM-ROMS simulation clearly underestimates LPS over the head of BoB and in the AS while overestimating over Northeastern Hills of India and over Myanmar (Figure 10c). Similarly, the total number of ML were 227 and 156 with a seasonal average of 9.1 and 6.3 in the ERA5 (Figure 10d) and in the RSM-ROMS simulation (Figure 10e), respectively. The underestimation of the ML in the head BoB, along the foothills of Himalayas and over AS in the RSM-ROMS simulation are apparent in Figure 10f. The total number of MD in ERA5 is 139 with a seasonal average of 5.5 (Figure 10g) and in RSM-ROMS simulation it is 151 with a seasonal average of 6.0 (Figure 10h). The underestimation of the MD in the RSM-ROMS simulation is largely over the head BoB and in the AS with an overestimation along the foothills of Himalayas (Figure 10i). But the relatively lower bias in the counts of MD compared to that of ML in the RSM-ROMS simulation suggests that the likelihood of ML becoming MD is much higher in the model, especially over central India. The underestimation of the LPS in head BoB and in AS despite the warm bias of SST and relatively weak bias of the 850 hPa winds in the RSM-ROMS simulation, could be related to errors in the zonal shear emanating from the westerly bias in the tropical easterly jet (not shown). The tropical easterly jet is weak in the R2 reanalysis that is further amplified in the RSM-ROMS simulation. The strong westward zonal wind shear of the SASM is found to be critical for the development of LPS (Goswami et al., 1980; Praveen et al., 2015; Sandeep & Ajayamohan, 2015), which unfortunately happens to be comparatively weak in the RSM-ROMS simulation (not shown). Nonetheless, the verification of these statistics of the seasonal activity of the LPS from the RSM-ROMS simulation is extremely encouraging given the disparity in reanalyses (Vishnu et al., 2020) and in global models (Praveen et al., 2015).

Several studies have indicated a dominating influence of the BSISO on the LPS (Chen & Weng, 1999; Goswami et al., 2003; Karmakar et al., 2021; Krishnamurthy & Ajayamohan, 2010; Yoon & Chen, 2005). Krishnamurthy and Ajayamohan (2010) indicate that there are nearly twice as many LPS days during active relative to the break phases of the BSISO. In Figure 11, we show the composite difference of the track density of the LPS between the wet and dry spells of the BSISO from ERA5 and the RSM-ROMS simulation. The LPS composites in Figures 11a–11c are based on the wet and dry spells of BSISO over central India (Figure 9a). Similarly, a comparable 20 year period (1991–2010) from RSM-ROMS simulation are used to develop the composite track density of LPS in Figures 11d–11f based on the wet and dry phases of the BSISO (Figure 9b). In both ERA5 and RSM-ROMS, the wet spells of the BSISO over central India produce a higher track density of LPS (i.e., a greater number of LPS per 1° × 1° grid) over the head waters of BoB than in dry spells (Figure 11). However, the model simulation displays a much smaller difference of the LPS track density over BoB and AS between the wet and dry

10.1029/2022JD037490

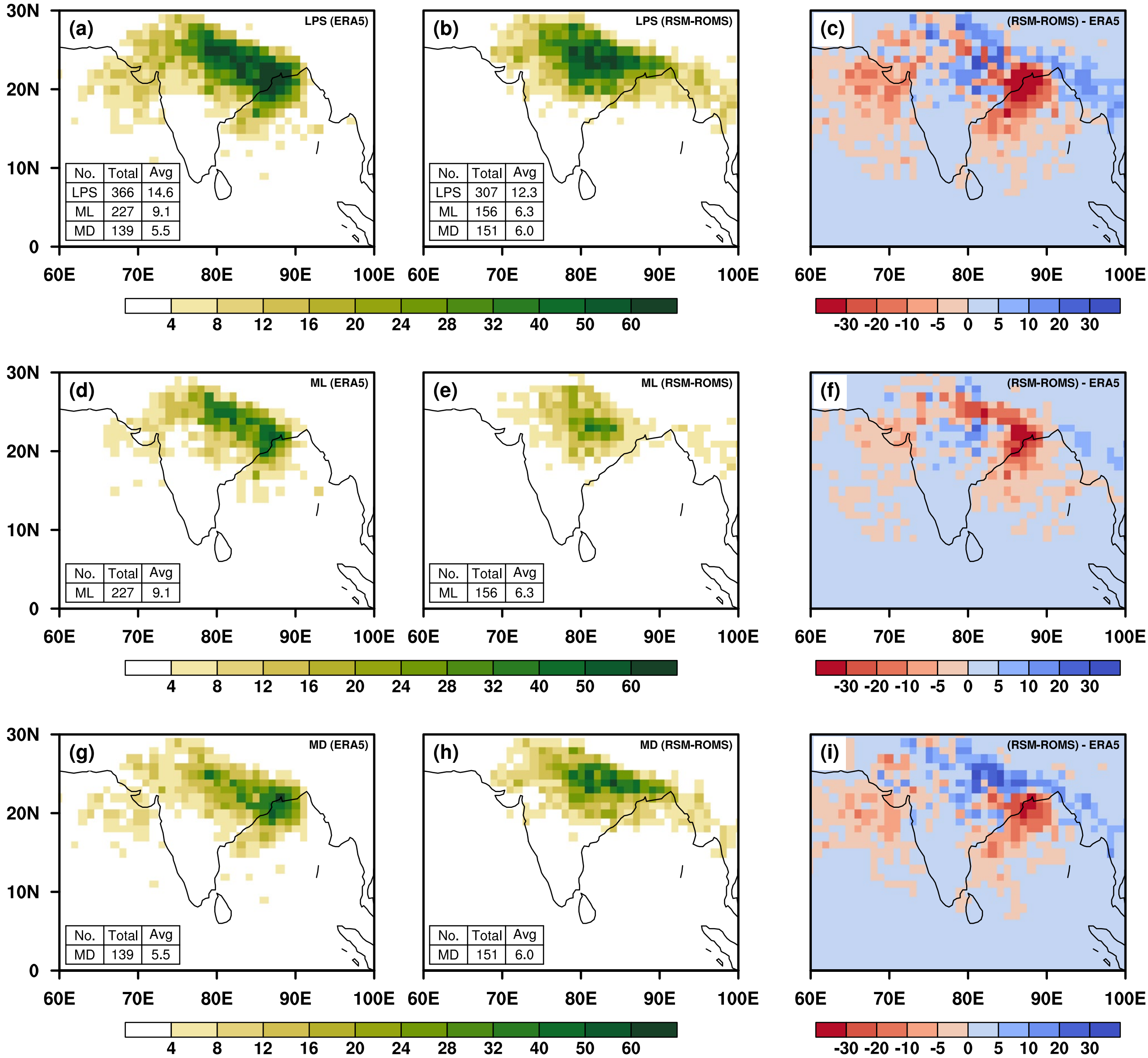

Figure 10. The track density of the Monsoon Low Pressure Systems (LPS) during June to September measured as number of LPS per 1° × 1° grid as diagnosed from (a) ERA5, (b) regional spectral model-regional ocean model (RSM-ROMS) simulation, and (c) the corresponding bias of RSM-ROMS over the period of 1986–2010. Similarly, the track density of monsoon lows (ML) from (d) ERA5, (e) RSM-ROMS, and (f) corresponding bias of RSM-ROMS. The track density of monsoon depressions (MD) from (g) ERA5, (h) RSM-ROMS, and (i) the corresponding bias of RSM-ROMS. The inset table in (a, b, d, e, g, and (h) provide the seasonal statistics of the total number (total) of LPS, ML, MD, and their seasonal average (Avg).

spells of the BSISO compared to ERA5. This is largely because the model has a bias of producing far fewer LPS over the oceans than ERA5 (Figure 10). Furthermore, the larger difference of the LPS track density between the wet and the dry spells of the BSISO is over central India in the model, which is further inland than in ERA5. But the negative difference of the track density along the foothills of the Himalayas suggesting higher LPS activity during the dry spell of the BSISO over central India is well simulated in the model.

10.1029/2022JD037490

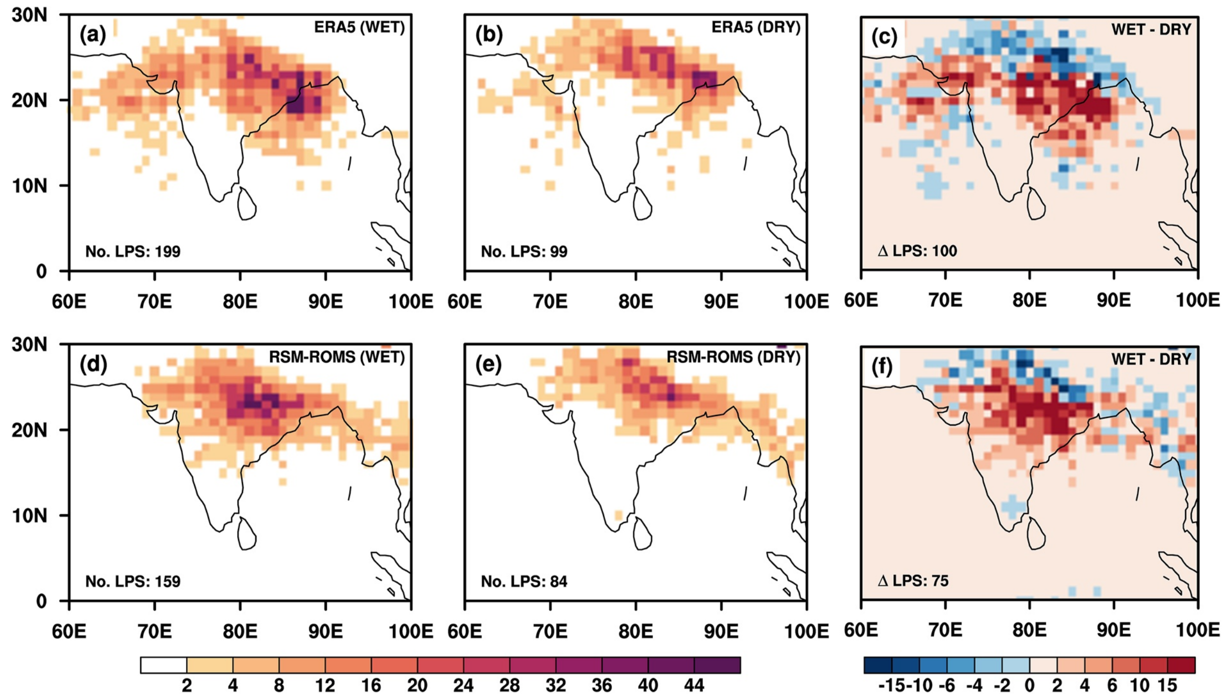

Figure 11. The composite track density of the monsoon low pressure systems (LPS) measured as number of LPS per 1° × 1° grid for (a), (d) wet spells and (b), (e) dry spells of the BSISO and their corresponding difference (c), (f) wet-dry from (a, b, c) ERA5 and (d, e, f) regional spectral model-regional ocean model (RSM-ROMS) simulation.

5. Conclusion

Generating a 20 km grid spacing simulation of the SASM climate from a 2.5° × 2.5° global atmospheric (R2) reanalysis and a 0.5° × 0.5° global oceanic (SODA) analysis that hosts a variety of temporal variations across many spatial scales poses a stiff challenge. In this study the fidelity of the RSM-ROMS simulation is assessed for its fidelity in simulating the features of the SASM. This paper highlights that at 20 km grid spacing, many of the topographic and bathymetric features of the domain appear realistic albeit, with their gradients best approximated at the discretized resolution of the regional model. The RSM-ROMS simulation shows reasonable fidelity of the seasonal climate of SASM. Like, the sharp topographic features of rainfall, the contrast of the convective activity between largely warm rain process in the ocean and mixed warm and cold rain process over land as witnessed from the distribution of frozen and unfrozen hydrometeors, and reduction in the bias of precipitable water over orographic features relative to R2.

The RSM-ROMS simulation clearly displays skill in describing the large-scale patterns of the upper ocean thermal structure that is consistent with the atmospheric forcing. For example, the shallow mixed layer and warmer SST in the equatorial Indian ocean that receives significant precipitation with weak surface westerlies in contrast to the deeper mixed layer and colder SST in the western AS under drier conditions and strong southwesterlies are nicely replicated in the downscaled simulation.

The fidelity of the SASM mean climate in the RSM-ROMS simulation provides confidence to further examine the sub-seasonal scales and extremes (like LPS) of the SASM. The intraseasonal oscillations of the SASM has been a difficult challenge for many climate models to simulate given its two distinct timescales of the BSISO (20–70 days) and QBM (10–20 days), their robust propagation, and their influence on LPS. The RSM-ROMS simulation impressively reproduces all these features including the northwest-southeast tilt of the BSISO and QBM. The simulation clearly shows the observed modulation of the LPS at the BSISO timescales. The LPS of the SASM form in a high vertical shear environment and largely intensify inland, confounding usual theories of tropical cyclone development. The inland intensification of the LPS is reproduced in the RSM-ROMS simulation.

The added value of the RSM-ROMS simulation of the SASM to the R2 global reanalysis is amply demonstrated in this paper. The intra-seasonal variations of the SASM and its defining features are important in defining their influence on the LPS. At 2.5° × 2.5°, the R2 reanalysis is simply too coarse to resolve the LPS and therefore the RSM-ROMS simulation clearly demonstrates its added value from permitting them at 20 km spatial resolution with reasonable seasonal statistics. However, the successful simulation of such mesoscale features by a regional climate model also leads to reasonable simulation of the complex, large-scale SASM climate. For example, the northwest-southeast tilt of the BSISO is associated with the northwestward track of the LPS (Karmakar & Misra, 2020; Karmakar et al., 2021). Similarly, the contrast in convection between BoB and central India is associated with the strengthening and propagation of the LPS inland. Such intricate relationships are not discernible in R2 reanalysis, which is available on a 2.5° × 2.5° grid.

This study is unique in many aspects. The analysis in this study stems from the longest (25-year) integration at 20 km horizontal resolution simulation of the SASM thus far (comparing recent studies like Rao et al., 2019; Varghese et al., 2019). The veracity of the BSISO and QBM in the RSM-ROMS simulation is unique as most climate models fail to get either its tilt or its propagation correctly (Konda & Vissa, 2022). The fidelity of the simulation in the statistics of the LPS and its variation with BSISO is also unique to this study. By way of the inclusion of air-sea coupling in RSM-ROMS, a comprehensive and dynamically consistent data set of the atmosphere and ocean at high resolution is generated for the SASM that is otherwise available only for the atmosphere or for the ocean from the atmospheric only or the ocean only reanalysis products, respectively.

From this study, we show that this RSM-ROMS simulation would be an ideal platform to launch intensive diagnostic studies to understand the BSISO's and their influence on LPS. Furthermore, given the fidelity of RSM-ROMS in simulating SASM as demonstrated from this work, future studies with RSM-ROMS forced with global model projections of the future climate would be of significant interest to understand the changes in some of these SASM features. However, the dry precipitation bias over BoB, the dry bias in precipitable water across the domain, warm bias of SST, and the deeper than observed sub-surface ocean (thermocline) over the equatorial Indian Ocean of the RSM-ROMS simulation cannot be ignored. Improving the simulation further with incorporating more processes (e.g., river routing and discharging into the ocean) that could potentially change the stratification of the upper ocean in BoB and thereby affect the air-sea fluxes and influence atmospheric convection, increasing the resolution to resolve the topographic and bathymetric features better, improving the physics (e.g., by including more sophisticated microphysics) that can affect the rendition of the mixed phase and cold rain processes better, and tuning the mixing in the ocean model could be part of future efforts.

Data Availability Statement

The IMERG rainfall from NASA was obtained from (IMERG, 2022). The ERA5 reanalysis data was from (ERA5, 2022), the mixed layer depth from Argo was obtained from (Holte et al., 2017) and the SODA v2.2.4 ocean reanalysis data was obtained from SODA (2022). The NCEP-DOE (R2) reanalysis data at 6 hourly interval was obtained from UCAR (2022) or alternatively the data can also be accessed from PSL (2022). The data from the RSM-ROMS integration to generate the figures in the manuscript are available from Misra et al. (2022). Figures 1, 2, and 5 were made with Grid Analysis and Display System Version 2.1.1.b0 licensed by George Mason University. Multichannel singular spectrum analysis (MSSA) carried out for generating Figures 8 and 9 is using Matlab version R2020a (MATLAB, 2020) under FSU license 731,138. The remaining figures in the paper were made with NCAR Command Language Version 6.6.2 licensed by UCAR. Track density is estimated using the tempestextremes software, which can be obtained from Tempestextremes (2022).

Acknowledgments
We acknowledge the support from NASA Grant 80NSSC19K1199 and 80NSSC22K0595.

References

Ajayamohan, R. S., Annamalai, H., Luo, J.-J., Hafner, J., & Yamagata, T. (2011). Poleward propagation of boreal summer intraseasonal oscillations in a coupled model: Role of internal processes. *Climate Dynamics*, *37*, 851–867. https://doi.org/10.1007/s00382-010-0839-6

Allen, M., & Robertson, A. (1996). Distinguishing modulated oscillations from coloured noise in multivariate datasets. *Climate Dynamics*, *12*, 775–784. https://doi.org/10.1007/s003820050142

Alpert, J. C., Kanamitsu, M., Caplan, P. M., Sela, J. G., White, G., & Kalnay, E. (1988). Mountain induced gravity wave drag parameterization in the NMC medium-range forecast model. *SAVE Proceedings of 8th Conference on Numerical Weather Prediction*, (pp. 726–733). American Meteorological Society.

Avila, E. E., & Caranti, G. M. (1994). A laboratory study of static charging by fracture in ice growing by riming. *Journal of Geophysical Research*, *99*, 10611–10620. https://doi.org/10.1029/93jd02926

Bhaskaran, B., Murphy, J. M., & Jones, R. G. (1998). Intraseasonal oscillation in the Indian summer monsoon simulated by global and nested regional climate models. *Monthly Weather Review*, *126*(12), 3124–3134. https://doi.org/10.1175/1520-0493(1998)126<3124:ioitis>2.0.co;2

Bhate, J., Unnikrishnan, C. K., & Rajeevan, M. (2012). Regional climate model simulations of the 2009 Indian summer monsoon. *Indian. IJRPS*, *41*(4), 488–500.

Carey, L. D., Rutledge, S. A., & Petersen, W. A. (2003). The relationship between severe weather reports and cloud-to-ground lightning polarity in the contiguous United States from 1989 to 1998. *Monthly Weather Review*, *131*, 1211–1228. https://doi.org/10.1175/1520-0493(2003)131<1211:trbssr>2.0.co;2

Carton, J. A., & Giese, B. S. (2008). A reanalysis of ocean climate using Simple Ocean Data Assimilation (SODA). *Monthly Weather Review*, *136*, 2999–3017. https://doi.org/10.1175/2007MWR1978.1

Chen, T.-C., & Weng, S.-P. (1999). Interannual and intraseasonal variations in monsoon depressions and their westward-propagating predecessors. *Monthly Weather Review*, *127*, 1005–1020. https://doi.org/10.1175/1520-0493(1999)127<1005:iaivim>2.0.co;2

Chen, X., Leung, L. R., Feng, Z., Song, F., & Yang, Q. (2021). Mesoscale convective systems dominate the energetics of the south Asian Summer Monsoon onset. *Geophysical Research Letters*, *48*, e2021GL094873. https://doi.org/10.1029/2021GL094873

Chen, X., Zhang, F., & Ruppert, J. H. (2019). Modulations of the diurnal cycle of coastal rainfall over south China caused by the boreal summer intraseasonal oscillation. *Journal of Climate*, *32*, 2089–2108. https://doi.org/10.1175/JCLI-D-18-0786.1

Chou, M. D., & Lee, K. T. (1996). Parameterizations for the absorption of solar radiation by water vapor and ozone. *Journal of the Atmospheric Sciences*, *53*, 1203–1208. https://doi.org/10.1175/1520-0469(1996)053<1203:pftaos>2.0.co;2

Chou, M. D., & Suarez, M. J. (1994). An efficient thermal infrared radiation parameterization for use in general circulation models. *NASA Technical Memorandum NASA-TM-104606*, *3*, 98. Retrieved from https://ntrs.nasa.gov/archive/nasa/casi.ntrs.nasa.%20gov/19950009331.pdf

Christensen, J. H., Carter, T. R., Rummukainen, M., & Amanatidis, G. (2007). Evaluating the performance and utility of regional climate models: The PRUDENCE project. *Climatic Change*, *81*(Suppl), 1–6. https://doi.org/10.1007/s10584-006-9211-6

Christensen, J. H., Machenhauer, B., Jones, R. G., Schär, C., Ruti, P. M., Castro, M., & Visconti, G. (1997). Validation of present-day regional climate simulations over Europe: LAM simulations with observed boundary conditions. *Climate Dynamics*, *13*, 489–506. https://doi.org/10.1007/s003820050178

Danielson, J. J., & Gesch, D. B. (2011). Global multi-resolution terrain elevation data (Open-File Report 2011–1073). https://doi.org/10.3133/ofr20111073

Dee, D., Uppala, S., Simmons, A., Berrisford, P., Poli, P., Kobayashi, S., et al. (2011). The ERA-interim reanalysis: Configuration and performance of the data assimilation system. *Quarterly Journal of the Royal Meteorological Society*, *137*(656), 553–597. https://doi.org/10.1002/qj.828

Ek, M. B., Mitchell, K. E., Lin, Y., Rogers, E., Grunmann, P., Koren, V., et al. (2003). Implementation of Noah land surface model advances in the National Centers for Environmental Prediction operational mesoscale Eta model. *Journal of Geophysical Research*, *108*, 8851, https://doi.org/10.1029/2002JD003296

Ezer, T., Arango, H., & Shchepetkin, A. F. (2002). Developments in terrain-following ocean models: Intercomparisons of numerical aspects. *Ocean Modelling*, *4*, 249–267. https://doi.org/10.1016/s1463-5003(02)00003-3

Fletcher, J. K., Parker, D. J., Turner, A. G., Menon, A., Martin, G. M., Birch, C. E., et al. (2018). The dynamic and thermodynamic structure of the monsoon over southern India: New observations from the INCOMPASS IOP. *Quarterly Journal of the Royal Meteorological Society*. https://doi.org/10.1002/qj.3439

Ghil, M., Allen, M. R., Dettinger, M. D., Ide, K., Kondrashov, D., Mann, M. E., et al. (2002). Advanced spectral methods for climatic time series. *Reviews of Geophysics*, *40*, 1003. https://doi.org/10.1029/2000RG000092

Giorgi, F., Hewitson, B., Christensen, J., Hulme, M., Von Storch, H., Whetton, P., et al. (2001). Regional climate information: Evaluation and projections. In *Climate change 2001: The Scientific Basis* (pp. 739–768). Cambridge University Press.

Goswami, B. N. (2005). South Asian monsoon. In W. K. M. Lau & D. E. Walliser (Eds.), *Intraseasonal variability in the atmosphere-ocean climate system* (pp. 21–61). Springer.

Goswami, B. N., Ajayamohan, R. S., Xavier, P. K., & Sengupta, D. (2003). Clustering of synoptic activity by Indian summer monsoon intraseasonal oscillations. *Geophysical Research Letters*, *30*(8), 1431. https://doi.org/10.1029/2002GL016734

Goswami, B. N., Keshavamurthy, R. N., & Satyan, V. (1980). Role of barotropic, baroclinic, and barotropic-baroclinic instability for the growth of monsoon depressions and mid-tropospheric cyclones. *Proceedings of the Indian Academy of Sciences - Earth & Planetary Sciences*, *89*, 79–97. https://doi.org/10.1007/BF02841521

Haidvogel, D. B., Arango, H. G., Hedstrom, K., Beckmann, A., Malanotte-Rizzoli, P., & Shchepetkin, A. F. (2000). Model evaluation experiments in the North Atlantic Basin: Simulations in nonlinear terrain-following coordinates. *Dynamics of Atmospheres and Oceans*, *32*(3), 239–281. https://doi.org/10.1016/s0377-0265(00)00049-x

Ham, S., Yoshimura, K., & Li, H. (2016). Historical dynamical downscaling for East Asia with the atmosphere and ocean coupled regional model. *Journal of the Meteorological Society of Japan*, *94A*, 199–208. https://doi.org/10.2151/jmsj.2015-046

Hong, S. Y., & Pan, H. L. (1996). Nonlocal boundary layer vertical diffusion in a medium-range forecast model. *Monthly Weather Review*, *124*(10), 2322–2339. https://doi.org/10.1175/1520-0493(1996)124<2322:nblvdi>2.0.co;2

Hunt, K. M. R., & Fletcher, J. K. (2019). The relationship between Indian monsoon rainfall and low-pressure systems. *Climate Dynamics*, *53*, 1859–1871. https://doi.org/10.1007/s00382-019-04744-x

Hurley, J. V., & Boos, W. R. (2015). A global climatology of monsoon low-pressure systems. *Quarterly Journal of the Royal Meteorological Society*, *141*, 1049–1064. https://doi.org/10.1002/qj.2447

Jayasankar, C. B., Rajendran, K., & Surendran, S. (2018). Monsoon climate change projection for the orographic west coast of India using high-resolution nested dynamical downscaling model. *Journal of Geophysical Research: Atmospheres*, *123*(15), 7821–7838. https://doi.org/10.1029/2018JD028677

Juang, H. M., & Kanamitsu, M. (1994). The NMC nested regional spectral model. *Monthly Weather Review*, *122*, 3–26. https://doi.org/10.1175/1520-0493(1994)122<0003:tnnrsm>2.0.co;2

Kanamaru, H., & Kanamitsu, M. (2007). Scale-selective bias correction in a downscaling of global reanalysis using a regional model. *Monthly Weather Review*, *135*, 334–350. https://doi.org/10.1175/mwr3294.1

Kanamitsu, M., Ebusuzaki, W., Woollen, J., Yang, S.-K., Hnilo, J., Fiorino, M., & Potter, G. L. (2002). NCEP-DOE AMIP-II reanalysis (R-2). *Bulletin of the American Meteorological Society*, *83*, 1631–1643. https://doi.org/10.1175/bams-83-11-1631(2002)083<1631:nar>2.3.co;2

Kang, I. S., Jin, K., Wang, B., Lau, K. M., Shukla, J., Krishnamurthy, V., & Liu, Y. (2002). Intercomparison of the climatological variations of Asian summer monsoon precipitation simulated by 10 GCMs. *Climate Dynamics*, *19*, 383–395. https://doi.org/10.1007/s00382-002-0245-9

Karmakar, N., Boos, W., & Misra, V. (2021). Influence of intraseasonal variability on the development of monsoon depressions. *Geophysical Research Letters*, *48*, e2020GL090425. https://doi.org/10.1029/2020GL090425

Karmakar, N., & Misra, V. (2020). Differences in the northward propagation of convection over the Arabian Sea and Bay of Bengal during boreal summer. *Journal of Geophysical Research*, *125*, e2019JD031648. https://doi.org/10.1029/2019jd031648

Konda, G., & Vissa, N. K. (2022). Robustness of BSISO and air-sea interactions in the CMIP (Phase-6) models over the north Indian Ocean. *Dynamics of Atmosphered and Oceans*. In press. https://doi.org/10.1016/j.dynatmoce.2022.101316

Krishnamurthy, V., & Ajayamohan, R. S. (2010). Composite structure of monsoon low pressure systems and its relation to Indian rainfall. *Journal of Climate*, *23*, 4285–4305. https://doi.org/10.1175/2010jcli2953.1

Krishnamurthy, V., & Shukla, J. (2007). Intraseasonal and seasonally persisting patterns of Indian monsoon rainfall. *Journal of Climate*, *20*, 3–20. https://doi.org/10.1175/jcli3981.1

Krishnamurti, T. N., & Balme, H. N. (1976). Oscillations of a monsoon system. Part I. Observational aspects. *Journal of the Atmospheric Sciences*, *33*, 1937–1954. https://doi.org/10.1175/1520-0469(1976)033<1937:ooamsp>2.0.co;2

Krishnamurti, T. N., Oosterhof, D. K., & Mehta, A. V. (1988). Air-sea interaction on the time scale of 30–50 days. *Journal of the Atmospheric Sciences*, *45*, 1304–1322. https://doi.org/10.1175/1520-0469(1988)045<1304:aiotts>2.0.co;2

Kumar, K. K., Hoerling, M., & Rajagopalan, B. (2005). Advancing Indian monsoon rainfall predictions. *Geophysical Research Letters*, *32*, L08704. https://doi.org/10.1029/2004GL021979

Lang, T. J., & Rutledge, S. A. (2002). Relationships between convective storm kinematics, precipitation, and lightning. *Monthly Weather Review*, *130*(10), 2492–2506. https://doi.org/10.1175/1520-0493(2002)130<2492:rbcskp>2.0.co;2

Li, H., Kanamitsu, M., Hong, S.-Y., Yoshimura, K., Cayan, D. R., & Misra, V. (2014a). A high-resolution ocean-atmosphere coupled downscaling of the present climate over California. *Climate Dynamics*, *42*(3–4), 701–714. https://doi.org/10.1007/s00382-013-1670-7

Li, H., Kanamitsu, M., Hong, S.-Y., Yoshimura, K., Cayan, D. R., Misra, V., & Sun, L. (2014b). Projected climate change scenario over California by a regional ocean-atmosphere coupled model system. *Climatic Change*, *122*(4), 609–619. https://doi.org/10.1007/s10584-013-1025-8

Loschnigg, J., & Webster, P. J. (2000). A coupled ocean-atmosphere system of SST modulation for the Indian Ocean. *Journal of Climate*, *13*, 3342–3360. https://doi.org/10.1175/1520-0442(2000)013<3342:acoaso>2.0.co;2

Lucas, C., LeMone, M. A., & Zipser, E. J. (1994). Vertical velocity in oceanic convection off tropical Australia. *Journal of the Atmospheric Sciences*, *51*(21), 3183–3193. https://doi.org/10.1175/1520-0469(1994)051<3183:vvioco>2.0.co;2

Maharana, P., & Dimri, A. P. (2016). Study of intraseasonal variability of Indian summer monsoon using a regional climate model. *Climate Dynamics*, *46*, 1043–1064. https://doi.org/10.1007/s00382-015-2631-0

Mandke, S. K., Pillai, P. A., & Sahai, A. K. (2020). Simulation of the monsoon intra-seasonal oscillations in Geophysical Fluid Dynamics Laboratory models from Atmospheric model intercomparison project integrations of coupled model model intercomparison project phase 5. *International Journal of Climatology*. https://doi.org/10.1002/joc.6536

Mearns, L. O., Arritt, R., Biner, S., & Bukovsky, M. S. (2012). The North American regional climate change assessment program: Overview of phase I results. *Journal of Climate*, 1337–1362. https://doi.org/10.1175/BAMS-D-11-00223.1

Meehl, G. (1987). The annual cycle and interannual variability in the tropical Pacific and Indian ocean regions. *Monthly Weather Review*, *115*, 27–50. https://doi.org/10.1175/1520-0493(1987)115<0027:tacaiv>2.0.co;2

Mellor, G. L., & Yamada, T. (1982). Development of a turbulence closure model for geophysical fluid problems. *Reviews of Geophysics*, *20*(4), 851–875. https://doi.org/10.1029/rg020i004p00851

Misra, V. (2008). Coupled interactions of the monsoons. *Geophysical Research Letters*, *35*, L12705. https://doi.org/10.1029/2008GL033562

Misra, V., Jayasankar, C. B., Mishra, A. K., Mitra, A. K., & Murugavel, P. (2022). Datasets from regional coupled ocean-atmosphere model (RSM-ROMS) over South Asia. OSF. https://doi.org/10.17605/OSF.IO/2YK64

Misra, V., Mishra, A., & Bhardwaj, A. (2017). High resolution regional coupled ocean-atmosphere simulation of the Indian summer monsoon. *International Journal of Climatology*, *37*(51), 717–740. https://doi.org/10.1002/joc.5034

Misra, V., Mishra, A., & Bhardwaj, A. (2018). Simulation of the Intraseasonal variations of the Indian summer monsoon in a regional coupled ocean-atmosphere model. *Journal of Climate*, 3167–3185. https://doi.org/10.1175/JCLI-D-17-0434.1

Mohr, K. I., Famiglietti, J. S., & Zipser, E. J. (1999). The contribution to tropical rainfall with respect to convective system type, size, and intensity estimated from the 85-GHz Ice Scattering Signature. *Journal of Applied Meteorology and Climatology*, *38*, 596–606. https://doi.org/10.1175/1520-0450(1999)038<0596:tcttrw>2.0.co;2

Monteguet, C. B., Madec, G., Fishcher, A. S., Lazar, A., & Ludicone, D. (2004). Mixed layer depth over the global ocean: An examination of profile data and a profile-based climatology. *Journal of Geophysical Research*, *109*, C12003. https://doi.org/10.1029/2004JC002378

Moorthi, S., & Suarez, M. J. (1992). Relaxed Arakawa-Schubert. A parameterization of moist convection for general circulation models. *Monthly Weather Review*, *120*(6), 978–1002. https://doi.org/10.1175/1520-0493(1992)120<0978:rasapo>2.0.co;2

Moron, V., Robertson, A., & Ghil, M. (2012). Impact of the modulated annual cycle and intraseasonal oscillation on daily-to-interannual rainfall variability across monsoonal India. *Climate Dynamics*, *38*, 2409–2435. https://doi.org/10.1007/s00382-011-1253-4

Murakami, T. (1976). Analysis of summer monsoon fluctuations over India. *Journal of the Meteorological Society of Japan*, *54*, 15–31. https://doi.org/10.2151/jmsj1965.54.1_15

Murugavel, P., Prabha, T. V., Pandithurai, G., Gopalkrishnan, V., & Pawar, S. D. (2021). Physical mechansims associated with the intense lightning over Indian region. *International Journal of Climatology*, *42*(8), 4300–4315. https://doi.org/10.1002/joc.7466

Nesbitt, S. W., Zipser, E. J., & Cecil, D. J. (2000). A census of precipitation features in the Tropics using TRMM: Radar, ice scattering, and ice observations. *Journal of Climate*, *13*, 4087–4106. https://doi.org/10.1175/1520-0442(2000)013<4087:acopfi>2.0.co;2

Noska, R., & Misra, V. (2016). Characterizing the onset and the demise of the Indian summer monsoon. *Geophysical Research Letters*, *43*(9), 4547–4554. https://doi.org/10.1002/2016GL068409

Petersen, W. A., & Rutledge, S. A. (1998). On the relationship between cloud-to-ground lightning and convective rainfall. *Journal of Geophysical Research*, *103*, 14025–14040. https://doi.org/10.1029/97jd02064

Praveen, V., Sandeep, S., & Ajayamohan, R. S. (2015). On the relationship between mean monsoon precipitation and low pressure systems in climate model simulations. *Journal of Climate*, *28*, 5305–5324. https://doi.org/10.1175/jcli-d-14-00415.1

PSL. (2022). Retrieved from https://psl.noaa.gov/data/gridded/data.ncep.reanalysis2.html

Rajendran, K., & Kitoh, A. (2006). Modulation of tropical intraseasonal oscillations by atmosphere–ocean coupling. *Journal of Climate*, *19*, 366–391. https://doi.org/10.1175/jcli3638.1

Rao, S. A., Goswami, B. N., Sahai, A. K., & co-authors (2019). Monsoon mission: A targeted activity to improve monsoon prediction across scales. *Bulletin of the American Meterological Society*, 2509–2532. https://doi.org/10.1175/BAMS-D-17-0330.1

Samala, B. K., Banerjee, S., Kaginalkar, A., & Dalvi, M. (2013). Study of the Indian summer monsoon using WRF–ROMS regional coupled model simulations. *Atmospheric Science Letters*, *14*, 20–27. https://doi.org/10.1002/asl2.409

Sandeep, S., & Ajayamohan, R. S. (2015). Poleward shift in Indian summer monsoon low level jetstream under global warming. *Climate Dynamics*, *45*, 337–351. https://doi.org/10.1007/s00382-014-2261-y

Selman, C., & Misra, V. (2015). Simulating diurnal variations over the southeastern United States. *Journal of Geophysical Research: Atmospheres*, *120*, 180–198. https://doi.org/10.1002/2014JD021812

Sengupta, D., Goswami, B. N., & Senan, R. (2001). Coherent intraseasonal oscillations of ocean and atmosphere during the Asian summer monsoon. *Geophysical Research Letters*, *28*, 4127–4130. https://doi.org/10.1029/2001gl013587

Shchepetkin, A. F., & McWilliams, J. C. (2005). The regional oceanic modeling system (ROMS): A split-explicit, free-surface, topography-following-coordinate oceanic model. *Ocean Modelling*, *9*(4), 347–404. https://doi.org/10.1016/j.ocemod.2004.08.002

Sikka, D. R. (2006). *A study on the monsoon low-pressure systems over the Indian Region and their Relationship with Drought and Excess Monsoon Seasonal Rainfall (Technical Report No. 217*, (p. 61). Center for Ocean-Land-Atmosphere Studies.

Sikka, D. R., & Gadgil, S. (1980). On the maximum cloud zone and the ITCZ over India longitude during the Southwest monsoon. *Monthly Weather Review*, *108*, 1840–1853. https://doi.org/10.1175/1520-0493(1980)108<1840:otmcza>2.0.co;2

Slingo, J. M., Sperber, K. R., Boyle, J. S., Ceron, J.-P., Dix, M., Dugas, B., et al. (1996). Intraseasonal oscillations in 15 atmospheric general circulation models: Results from an AMIP diagnostic subproject. *Climate Dynamics*, *12*, 325–357. https://doi.org/10.1007/bf00231106

SODA. (2022). Retrieved from https://iridl.ldeo.columbia.edu/SOURCES/.CARTON-GIESE/.SODA/.v2p2p4/?Set-Language=en

Tempestextremes. (2022). Retrieved from https://github.com/ClimateGlobalChange/tempestextremes

Tiedtke, M. (1983). The sensitivity of the time-mean large-scale flow to cumulus convection in the ECMWF model. In *Proceedings of ECMWF Workshop on convective in large-scale models* (pp. 297–316). European Centre for Medium-Range Weather Forecasts.

UCAR. (2022). Retrieved from https://rda.ucar.edu/datasets/ds091.0/

Ullrich, P. A., & Zarzycki, C. M. (2016). TempestExtremes v1.0: A framework for scale-insensitive pointwise feature tracking on unstructured grids. *Geoscientific Model Development Discussions*. https://doi.org/10.5194/gmd-2016-217

Umlauf, L., & Burchard, H. (2003). A generic length-scale equation for geophysical turbulence models. *Journal of Marine Research*, *61*(2), 235–265. https://doi.org/10.1357/002224003322005087

Varghese, S. J., Surendran, S., Rajendran, K., & Kitoh, A. (2019). Future projections of Indian summer monsoon under multiple RCPs using a high resolution global climate model multiforcing ensemble simulations. *Climate Dynamics*, *54*, 1315–1328. https://doi.org/10.1007/s00382-019-05059-7

Vishnu, S., Boos, W. R., Ullrich, P. A., & O'Brien, T. A. (2020). Assessing historical variability of South Asian monsoon lows and depressions with an optimized tracking algorithm. *Journal of Geophysical Research: Atmospheres*, *125*, e2020JD032977. https://doi.org/10.1029/2020JD032977

Wang, B., An, S.-I., & Li, T. (2003). Atmosphere–warm ocean interactionand its impact on Asian–Australian Monsoon variation. *Journal of Climate*, *16*, 1195–1211. https://doi.org/10.1175/1520-0442(2003)16<1195:aoiaii>2.0.co;2

Wang, B., Kang, I.-S., & Lee, J.-Y. (2004). Ensemble simulationsof Asian–Australian Monsoon variability by 11 AGCMs. *Journal of Climate*, *17*, 803–818. https://doi.org/10.1175/1520-0442(2004)017<0803:esoamv>2.0.co;2

Webster, P. J., & Hoyos, C. (2004). Prediction of monsoon rainfall and river discharge on 15–30-day time scales. *Bulletin of the American Meteorological Society*, *85*, 1745. https://doi.org/10.1175/BAMS-85-11-1745

Webster, P. J., Magana, V. O., Palmer, T. N., Shukla, J., Tomas, R. A., Yanai, M., & Yasunari, T. (1998). Monsoons: Processes, predictability, and the prospects for prediction. *Journal of Geophysical Research*, *103*, 14451–14510. https://doi.org/10.1029/97jc02719

Williams, E., Mushtak, V., Rosenfeld, D., Goodman, S., & Boccippio, D. (2005). Thermodynamic conditions favorable to superlative thunderstorm updraft, mixed phase microphysics and lightning flash rate. *Atmospheric Research*, *76*, 288–306. https://doi.org/10.1016/j.atmosres.2004.11.009

Wu, R., & Kirtman, B. (2005). Roles of Indian and Pacific Oceanair–sea coupling in tropical atmospheric variability. *Climate Dynamics*, *25*, 155–170. https://doi.org/10.1007/s00382-005-0003-x

Wu, R., Kirtman, B. P., & Pegion, K. (2008). Local rainfall-SST relationship on subseasonal time scales in satellite observations and CFS. *Geophysical Research Letters*, *35*, L22706. https://doi.org/10.1029/2008GL035883

Yasunari, T. (1979). Cloudiness fluctuations associated with the northern hemisphere summer season. *Journal of the Meteorological Society of Japan*, *57*, 227–242. https://doi.org/10.2151/jmsj1965.57.3_227

Yasunari, T. (1980). A quasi-stationary appearance of 30 to 40 day period in the cloudiness fluctuations during the summer monsoon over India. *Journal of the Meteorological Society of Japan*, *58*, 225–229. https://doi.org/10.2151/jmsj1965.58.3_225

Yasunari, T. (1981). Structure of an Indian summer monsoon system with around 40-day period. *Journal of the Meteorological Society of Japan*, *59*, 336–354. https://doi.org/10.2151/jmsj1965.59.3_336

Yoon, J.-H., & Chen, T.-C. (2005). Water vapor Budget of the Indian monsoon depression. *Tellus*, *57A*, 770–782. https://doi.org/10.1111/j.1600-0870.2005.00145.x

Zhao, Q., & Carr, F. H. (1997). A prognostic cloud scheme for operational NWP models. *Monthly Weather Review*, *125*(8), 1931–1953. https://doi.org/10.1175/1520-0493(1997)125<1931:apcsfo>2.0.co;2

Zipser. (2003). *Some views on "Hot Towers" after 50 years of tropical field programs and two years of TRMM data.Cloud systems* (pp. 49–58). American Meteorological Society. https://doi.org/10.1007/978-1-878220-63-9_5

Zipser, E. J., Cecil, D. J., Liu, C., Nesbitt, S. W., & Yorty, D. P. (2006). Where are the most intense thunderstorms on Earth? *Bulletin of the American Meterological Society*, 1057–1071. https://doi.org/10.1175/BAMS-87-8-1057

Zou, L., & Zhou, T. (2016). A Regional Ocean–atmosphere coupled model developed for CORDEX East Asia: Assessment of Asian summer monsoon simulation. *Climate Dynamics*, *12*, 3627–3640. https://doi.org/10.1007/s00382-016-3032-8

References From the Supporting Information

Abarca, S. F., Corbosiero, K. L., & Galarneau, T. J., Jr. (2010). An evaluation of the worldwide lightning location network (WWLLN) using the national lightning detection network (NLDN) as ground truth. *Journal of Geophysical Research*, *115*, D18206. https://doi.org/10.1029/2009jd013411

Dowden, R. L., Brundell, J. B., & Rodger, C. J. (2002). VLF lightning location by time of group arrival (TOGA) at multiple sites. *Journal of Atmospheric and Solar-Terrestrial Physics*, *64*, 817–830. https://doi.org/10.1016/s1364-6826(02)00085-8

Hersbach, H., Bell, W., Berrisford, P., Horanyi, A., Sabater, J. M., Nicolas, J., et al. (2019). The ERA5 global reanalysis. *Quarterly Journal of the Royal Meteorological Society*, *146*, 1999–2049. https://doi.org/10.1002/qj.3803

Holte, J., Talley, L. D., Gilson, J., & Roemmich, D. (2017). An Argo mixed layer climatology and datasbase. *Geophysical Research Letters*, *44*, 5618–5626. https://doi.org/10.1002/2017gl073426

Huffman, G. J., Stocker, E. F., Bolvin, D. T., Nelkin, E. J., & Tan, J. (2019). *GPM IMERG final precipitation L3 half hourly 0.1 degree x 0.1 degree V06*. Goddard Earth Sciences Data and Information Services Center (GES DISC). https://doi.org/10.5067/GPM/IMERG/3B-HH/06

Reynolds, R. W., Smith, T. M., Liu, C., Chelton, D. B., Casey, K. S., & Schlax, M. G. (2007). Daily high-resolution-blended analyses for sea surface temperature. *Journal of Climate*, *20*, 5473–5496. https://doi.org/10.1175/2007jcli1824.1

Supplementary Material

Dynamic Downscaling the South Asian Summer Monsoon from a Global Reanalysis using a Regional Coupled Ocean-Atmosphere Model

Vasubandhu Misra[1, 2, 3, #], C. B. Jayasankar[2, 3], A. K. Mishra[4, 5], A. Mitra[5], and P. Murugavel[6, 7]

[1]Department of Earth, Ocean and Atmospheric Science, Florida State University, Tallahassee, Florida, U.SA.

[2]Center for Ocean-Atmospheric Prediction Studies, Florida State University, Tallahassee, Florida, U.SA.

[3]Florida Climate Institute, Florida State University, Tallahassee, Florida, U. S. A.

[4]Ministry of Earth Sciences, India

[5]National Center for Medium Range Weather Forecasting, New Delhi, India

[6]Indian Institute of Tropical Meteorology, Pune, India

[7]Savitribai Phule Pune University, Pune, India

Corresponding Author Email: vmisra@fsu.edu

Table S1: Details of the verification datasets used in the study

Variable	Source	Purpose	Spatial resolution	Period used in the study
Rainfall	IMERG (Huffmann et al. 2019)	Verification of seasonal mean, interannual and intraseasonal variations over both land and ocean	0.1° x 0.1°	2001-2020
Lightning strokes	WWLLN (http://wwlln.net; (Dowden et al. 2002 and Abarca et al. 2010)	Verification of frozen precipitable water	0.25° x 0.25°	2010-2019
Upper air variables	ERA5 (Hersbach et al. 2019)	Verification of seasonal mean 850hPa winds, precipitable water	0.25° x 0.25°	1986-2010
SST	OISSTv2 (Reynolds et al. 2007)	Verification of seasonal mean SST and rainfall-SST relationship	0.25° x 0.25°	1986-2010
Mixed layer depth	Argo (Holte et al. 2017)	Verification of seasonal mean mixed layer depth	1° x 1°	2000-2020
Depth of the 20°C isotherm in the ocean	SODA reanalysis (Carton and Giese 2008)	Verification of the depth of the seasonal mean 20°C	0.5° x 0.5°	1986-2010

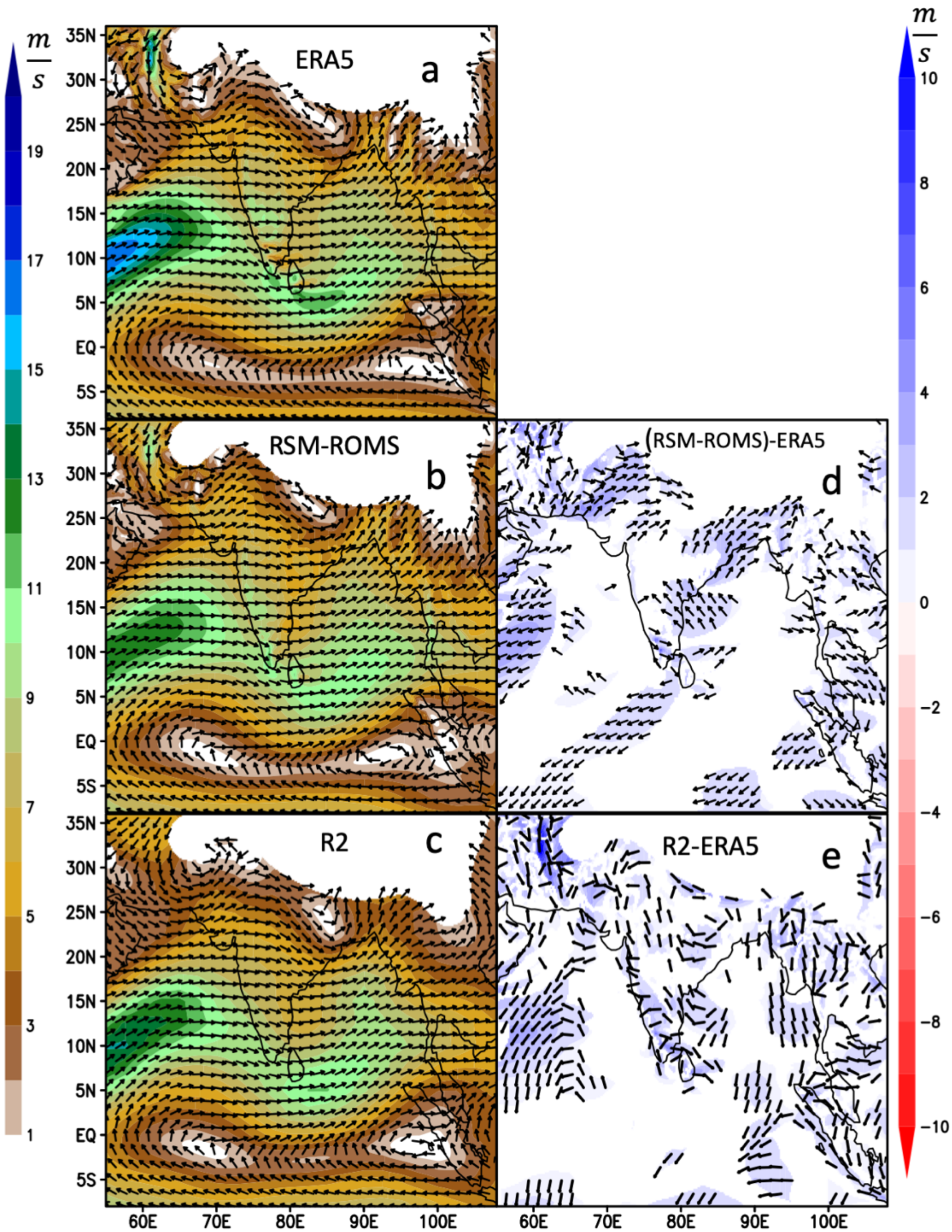

Figure S1: The climatological seasonal (May-June-July-August-September) mean 850hPa winds (m s^{-1}) from a) ERA5, b) RSM-ROMS, and c) R2 reanalysis. The corresponding systematic errors from c) RSM-ROMS and d) R2 reanalysis. Only statistically significant values at 95% confidence interval according to t-test is shown in (d) and (e).